Journal of Materials Processing Tech. 316 (2023) 117950

Contents lists available at ScienceDirect

Journal of Materials Processing Tech.

journal homepage: www.elsevier.com/locate/jmatprotec

Microstructure, microtexture, and crack susceptibility in pearlitic steel during lab-simulated processes aiming tensile armor application in flexible pipelines

Pablo B.P. Leão [a,*], Shutong Zhang [b], J.R. Barros Neto [c], Suyanny A. Freire [a], Rodrigo de C.P. Loureiro [a], Antonio J. Ramirez [b], H.F.G. de Abreu [a]

[a] *Department of Metallurgical and Materials Engineering, Universidade Federal do Ceará, Fortaleza, Brazil*
[b] *Materials Science and Engineering Department, The Ohio State University, Columbus, OH, USA*
[c] *Department of Materials Engineering, Universidade Federal do Piaui, Teresina, Brazil*

ARTICLE INFO

Associate Editor: Zhenshan Cui

Keywords:
Patenting
Cold-rolling
Pearlite
EBSD
Crack
Microtexture

ABSTRACT

Tensile armor is usually made of flat pearlitic steel wires and produced in a manufacturing sequence as follows: hot-rolling → patenting treatment (PT) → cold forming → wire coiling → stress relief → re-winding wire process. To evaluate the effect of the key parameters in this set of processes on the microstructure, microtexture, and crack susceptibility in commercial pearlitic steel, four process routes were lab-simulated with different setups of 45% hot-rolling, PT, and 65% cold-rolling. Subsequently, the cold-rolled specimens produced through the four distinct routes underwent two stress relief treatments (at 400 and 700 °C for 60 s), succeeded by simulation of the re-winding wire process via four alternated three-point bending procedures. Scanning electron microscope images, microhardness, and electron backscattered diffraction techniques were extensively performed in this work. Due to pearlitic block size control, the PT influenced the $\{111\}<112>$ component formation during the cold-rolling process. During the bending experiments, cracks were detected just in the route with the highest cold-rolled $\{111\}<112>$ microtexture orientation followed by stress relief at 700 °C. This crack susceptibility was related to the small recrystallized grains nucleated in the shear bands of the $\{111\}<112>$ pearlitic blocks during the stress relief treatment.

1. Introduction

The microstructure of fully pearlitic steels is generally composed of a lamellar arrangement of alternating soft ferrite (α) and hard cementite (θ) plates. According to Takahashi et al. (1978a),(1978b), the structure of lamellar pearlite can be defined in two hierarchical categories: pearlite colony and pearlite block (or nodule). Specifically, the pearlite colony is defined by the region that comprises the same direction of cementite lamellae, whereas zones with the identical crystallographic orientation of ferrite refer to a pearlite block that is developed from the prior austenite (γ) grain boundary. In this concern, the control of the Interlamellar Spacing (IS) of pearlite and the Prior Austenite Grain Size (PAGS) may result in an excellent combination of high strength and satisfactory ductility in pearlitic steel (Taleff et al., 2002). This mechanical relationship ascribes pearlitic steels to be required for many wire-related applications, such as suspension bridge cables, tire wires, piano wires, and even in the oil and gas sector as tensile armors in flexible pipelines (Barik et al., 2021; Tagliari et al., 2019).

Regarding tensile armor employment, flat pearlitic steel wires are twisted around the pipe in a helical shape forming a strong layer. This set of wires promotes axial rigidity while minimally compromising the pipeline flexibility, supporting all the pipeline weight and transferring the load to the vessel structure (Taleff et al., 2002). This complex steel performance requires strict control of microstructure and crystallographic orientation distribution, which are determined by parameters adopted during the manufacturing process. In this context, before the final application, the flat pearlitic steel wires can be industrially produced in the following route: hot-rolling process (HRP) → patenting treatment (PT) → cold forming (drawing, rolling, or drawing + rolling) → wire coiling → stress relief (recovery) heat treatment (EP 0 232 558 B1, 1990; EP 0 478 771 B1, 1996) → re-winding wire into bobbins (Fernando et al., 2017).

---

* Correspondence to: Campus Universitário do Pici Block 729 – Pici, Fortaleza 60020-181, CE, Brazil.
E-mail address: pablobruno@alu.ufc.br (P.B.P. Leão).

https://doi.org/10.1016/j.jmatprotec.2023.117950
Received 2 December 2022; Received in revised form 3 March 2023; Accepted 12 March 2023

Concerning PT, it provides the opportunity to optimize the strength/ductility ratio and also promotes a final homogeneous pearlitic microstructure. Firstly, this thermal treatment consists in austenitizing the steel in temperatures above 900 °C (EP 0 232 558 B1, 1990; EP 0 478 771 B1, 1996). This stage corresponds to direct control of the PAGS that is dependent on the austenitizing temperature and time (Sun et al., 2014). Saito et al. (2018) concluded that austenite nucleation sites in the previous structure of carbon steels are preferentially in the following sequence: ferrite/pearlite interfaces, pearlite block boundaries, and pearlite colony boundaries. In particular, the PAGS is related to influencing the ductility and impact toughness in pearlitic steels (Lewandowski and Thompson, 1986; Zhou et al., 2016). Conversely, the austenitic grain boundaries are also sites for pearlite nucleation. Consequently, the PAGS has a significant impact on the volume fraction of pearlite as well as the size of colonies (Porcaro et al., 2019) and blocks (Behera et al., 2019). In contrast, the IS is not controlled by the PAGS, instead, it is strongly regulated by the austenite-to-pearlite transformation temperature. This decomposition is a diffusion-controlled reaction. Thus, by lowering this transformation temperature, the distance of carbon diffusion will decrease, resulting in a thinner IS of pearlite (Aranda et al., 2014). Following the Hall-Petch relationship, it is well-known from the literature (Ohba et al., 2007) that the strength of pearlitic steels is correlated with the IS. In this way, the austenitization step is followed by a fast immersion of the steel into a molten bath (lead or salt) or fluidized bed for reducing the temperature of pearlite formation and ensuring an isothermal transformation (in the range of around 500–700 °C). Regarding environmental pollution and cooling rate performance, a molten salt is a reasonable option as a refrigerant bath for PT (Ohba et al., 2007; Bhole and Friedman, 2014). Also, Ohba et al. (2007) found better mechanical properties for pearlitic steel patented in salt baths in comparison to lead baths. In addition, the mechanical property of pearlitic steels produced via PT is desired for the following cold forming process, especially for higher reductions in the cold wire drawing process (Paris, 1996).

During cold forming, the complex structure of lamellar pearlite is usually related to undergoing inhomogeneous plastic deformation (localized strain zones). In this way, due to the lower yield strength of ferrite in comparison to cementite, the yielding in a pearlite colony may occur through plastic deformation predominantly in the ferrite matrix (Tomota et al., 2003). Furthermore, through measurements of in situ neutron diffraction during tensile deformation of pearlitic steel, Kanie et al. (2004) confirmed that cementite lamellae are in an elastic state at the moment the ferrite phase is under plastic deformation. In Body-Centered Cubic (BCC) metals, the cold plastic behavior can be described in terms of the pencil glide mechanism, where dislocation slip occurs on {110}, {112}, and {123} planes along the close-packed < 111 > direction (Kestens and Pirgazi, 2016). However, cementite lamellae can act as barriers against dislocation motion through the ferrite and consequently, pile-ups of dislocation may occur at the ferrite/cementite interface (Eshelby et al., 1951). Therefore, the heterogeneous strain distribution is dependent on the geometrical arrangement of cementite and the crystallographic orientation of ferrite in a pearlite colony (Yajima et al., 2021; Guo et al., 2014). To clarify, Teshima et al. (2017) observed the highest local strain in pearlite colonies aligned near 45° about the applied tensile stress due to the favorable ferritic dislocations gliding in this direction. Similarly, it has been pointed out by researchers (Guo et al., 2014; Durgaprasad et al., 2018) that during cold drawing pearlite colonies non-aligned to the drawing direction experience the highest degree of plastic deformation (especially at 45°). In addition, Durgaprasad et al. (2018) reported that the amount of plastic deformation in pearlite colonies is also affected by their IS. More specifically, Takahashi et al. (1978a),(1978b) described that in pearlites with refined structure, slips occur relatively homogeneously, while in coarse pearlites, slips are less uniformly distributed. Recently, Yajima et al. (2021) detected through the digital image correlation (DIC) method and tensile experiment that the boundaries of pearlite blocks are high-strain regions due to the anisotropic deformation among them. Furthermore, regarding the cold-rolling process, researchers (Furuhara et al., 2005; Zhang et al., 2007) noticed non-uniform distribution of pearlite colonies after a cold reduction of over 70%. In this context, the authors found three sorts of rolled pearlites (irregularly bent lamellae, coarse lamellae with shear band, and fine lamellae) which are a result of the initial deformation mode in different pearlite arrangements. Moreover, previous studies (Furuhara et al., 2005; Valiente et al., 2005) revealed that irregular strain distribution during cold deformation of pearlitic steel can collaborate for developing shear bands that are related to crack initiation.

Then, the cold-worked pearlitic steel wrapped in coils is usually subjected to recovery heat treatment that is generally performed below Ac1 temperature, in a vast range of temperatures (400–710 °C) and time (from a few seconds to several hours) (EP 0 478 771 B1, 1996; US 9.249.486 B2, 2016). In this regard, a partial restoration of mechanical properties occurs due to the rearrangement and annihilation of part of the dislocations (Humphreys et al., 2017). Subsequently, the wire is unwrapped from the coils, passed through pinch and casting rollers, and then, it is rewrapped onto bobbins. This operation causes an arduous plastic deformation into the material that is usually lab-simulated through bending experiments (Fernando et al., 2017). Finally, as tensile armor in flexible pipelines, the pearlitic rectangular wires are submitted to cyclic loading conditions and are exposed to a corrosive environment, which can assist the progress of fatigue cracks (Bai and Bai, 2005). Thus, it is paramount to identify and avoid manufacturing parameters that can provide crack events. Concerning specifically the aforementioned sequential processes for tensile armor application, the microstructural and crystallographic behavior of pearlitic steel in each of those process steps and together combined are not reported simultaneously in the literature. In this manner, this study mainly focuses on investigating the evolution of microstructure, microtexture, and crack formation in commercial pearlitic steel, regarding different manufacturing routes with variations of key parameters under laboratory scale. This lab manufacturing design was able to provide a harmful condition prone to crack formation. The microstructural and crystallographic assessments were conducted, respectively, by secondary electron (SE) image and electron backscattered diffraction (EBSD) techniques. Finally, this work can provide additional and relevant technical information for avoiding microstructural issues during the manufacturing of flat pearlitic steel wires.

2. Materials and methods

2.1. Samples processing

The four lab-simulated routes employed in this work are presented in Fig. 1. The chemical composition of the as-received pearlitic steel obtained by an optical emission spectrometer (THERMOARL 4460 M) is shown in Table 1. The dimensions of the starting steel samples were 8 mm (thickness) x 40 mm (length) x 50 mm (width). A laboratory scale rolling machine with 110 mm diameter rolls and a rolling speed of 8 m/min was employed in the rolling stages. An infrared thermometer was adopted for measuring the hot-rolling (immediately before the hot passes) and salt bath temperatures. Regarding the hot-rolling process in Fig. 1**(a)** and its detailed steps in Fig. 1**(b)**, the starting samples were austenitized at 1050 °C for 600 s in a muffle furnace, and after that, they were transferred instantly to the rolling machine for a hot pass of adjustment (≈0.03 mm of reduction). Subsequently, the samples were put back in the furnace at the same temperature (1050 °C) for 60 s followed by an additional hot pass (≈0.6 mm of reduction/pass). The last procedure was repeated six times up to ≈ 45% of thickness reduction (≈4.4 mm in final thickness) followed by air cooling. The average finish rolling temperature was 906 °C. This hot-rolling process was identically implemented at the beginning of the four routes. The hot-rolled specimen was named Sample 1 (S1) and it worked as an initial comparative

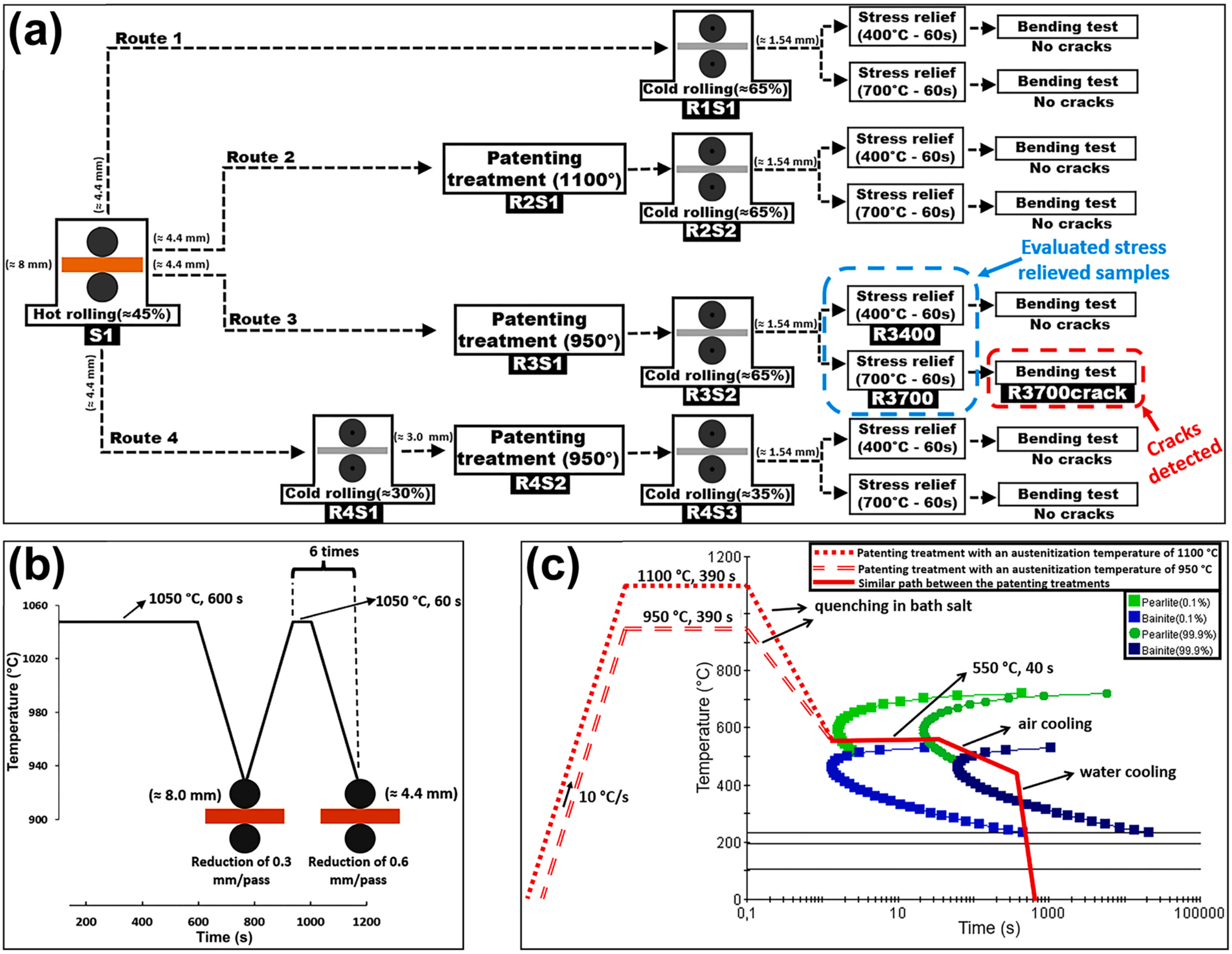

Fig. 1. Scheme of the four laboratory processing routes performed in the present work. (a) Overall flowchart representation of the process routes. (b) Illustrative diagram of the individual steps performed in the hot rolling (≈45) process. (c) Isothermal transformation diagram with representative details of the patenting treatments carried out in this study. The numbers in millimeters (mm) contained in Fig. 1(a) and 1 (b) represent the samples' thicknesses.

Table 1
Chemical composition of the as-received pearlitic steel (wt%).

C	Mn	Si	S	P	Cr	Ni	V	Al	Ti	Fe
0.736	**0.648**	**0.227**	**0.006**	**0.011**	**0.179**	**0.023**	**0.004**	**0.023**	**0.003**	**Bal.**

reference of microtexture and microstructure to the following step in each route.

Additionally, in this work, two PTs were carried out with two different austenitization temperatures (ATs), 1100 °C (Route 2 in Fig. 1 **(a)**) and 950 °C (Routes 3 and 4 in Fig. 1**(a)**) for 390 s both (as illustrated in Fig. 1**(c)**). Next, the samples were direct quenched in a bath salt (60% potassium nitrate + 40% sodium nitrate) at 550 °C for 40 s followed by air and water cooling. The specimens from these patented conditions were entitled, accordingly to their respective route and sample order, such as Route 2 - Sample 1 (R2S1), Route 3 - Sample 1 (R3S1), and Route 4 - Sample 2 (R4S2).

The cold-rolling process was performed by introducing many passes at room temperature (≈0.1 mm in thickness reduction/pass) until the aimed thickness (≈1.54 mm). In Route 1 - Sample 1 (R1S1), Route 2 – Sample 2 (R2S2), and Route 3 – Sample 2 (R3S2), the cold thickness reductions were executed from ≈ 4.4 mm up to ≈ 1.54 mm (≈65% of reduction). In contrast, in Route 4 the cold thickness reduction occurred in two moments; firstly, just after the HRP, in Route 4 - Sample 1 (R4S1) from ≈ 4.4 mm of thickness to ≈ 3 mm (≈30%), and secondly, after PT, in Route 4 – Sample 3 (R4S3) from ≈ 3 mm of thickness to ≈ 1.54 mm (≈35%), also resulting in ≈ 65% of cold reduction.

As shown in Fig. 1**(a)**, the 65% cold-reduced samples from the four different routes underwent stress relief heat treatments at 400 and 700 °C for 60 s. Then, for simulating the process of re-winding wire into bobbins, a three-point bending experiment at room temperature was applied in all the eight stress-relived conditions, using samples with dimensions of 1.54 × 12.5 × 60 mm^3 (the larger length was aligned to the rolling direction) (Fernando et al., 2017). The bending experiment was executed by a universal testing machine (landmark 370.10) with a maximum load of 100 kN. In addition, the rollers' diameter of the pins, the distance between support pins, the displacement rate, and the maximum displacement of the loading pin were, respectively, 10 mm, 40 mm, 2 mm/min, and 4.5 mm. This procedure was performed four times in all stress-relieved conditions alternating the superior and inferior sample's surfaces which were in contact with the pins. However, after the bending tests, cracks were only observed in the stress-relieved condition at 700 °C from Route 3, as indicated in Fig. 1**(a)**. In this regard, the stress-relieved and bent conditions evaluated in this work were only, respectively, from Route 3 (R3400 and R3700) and the cracked one (R3700crack).

2.2. Samples characterization

All the samples, except the cracked ones, were investigated in the sample's centroid region (in the middle thickness and width of the rectangular samples) and on the longitudinal section parallel to the rolling direction (RD). The samples were prepared through a regular metallographic procedure based on grinding (using sandpapers from #240 to #2000 grit) and polishing (using diamond suspensions of 6, 3, and 1 μm). Then, the specimens were etched in 4% Nital solution for microstructural SE observation through a field emission gun (FEG) THERMO SCIENTIFIC QUATTRO environmental scanning electron microscope (Quattro ESEM). An accelerating voltage of 20 kV and a beam current of 1.6 nA were adopted during the SE image acquisition. For crystallographic microtexture examinations, the samples were prepared with vibrometer polishing using 0.04 μm colloidal silica for two hours in addition to the grinding and polishing processes. The EBSD maps were acquired via the EDAX EBSD detector coupled with the Quattro ESEM. The EBSD analysis was carried out using an operating voltage of 20 kV, a step size of 50 nm, a working distance of 10 mm, and a sample tilt angle of 70°. The EBSD file evaluations were performed by OIM software. Inverse pole figure (IPF) maps were plotted in the Z-direction (sample's normal direction), while Taylor factor maps were calculated considering the $\{110\}< 111 >$ slip system and tensile loading in the longitudinal direction (parallel to the rolling direction). Moreover, the interlamellar spacing and pearlite colony size were measured from SE micrographs via ImageJ software.

Finally, microhardness measurements were accomplished using a Leco AMH43 automatic machine setting a load of 200 gf and a holding time of 10 s. On each sample, the indentations were performed in a 5 by 30 matrix with a spacing of 150 μm between them.

3. Results and discussion

3.1. Samples before 65% cold-rolling reduction

There are two main reasons for applying PT in pearlitic steels: refining and homogenizing the pearlitic microstructure which results in an optimization of mechanical properties. This section focuses on investigating the fundamental effects of PT on the microtexture and microstructure of pearlitic steel. Fig. 2 presents color-coded IPF maps and their respective orientation distribution function (ODF), of the samples under different setups of PT (R2S1, R3S1, R4S1, and R4S2), including the non-patenting treated one (S1). The ODF intensities are expressed in multiple random densities (mrd) and their main microtexture components are summarized in Table 2.

Additionally, the average pearlitic block size (PBS) measured from the IPF maps in Fig. 2 of the samples just before the final 65% cold-reduction (S1, R2S1, R3S1, and R4S2) is presented in Fig. 3 **(a)**. While Fig. 3 **(b)** exhibits the total length per area of the grain boundary types found in each IPF map provided in Fig. 2. Under the S1 condition (only hot-rolled), it was found the average PBS of 14.1 μm ± 1.2 μm, and the shaper ferritic orientation was the $\{001\}< 010 > \alpha$ (cube) component. In comparison to S1, the introduction of PT after the HRP decreased the average PBS to 9.9 μm ± 0.7 μm (R2S1) and 8.7 μm ± 1.1 μm (R3S1). It has been pointed out (Zhou et al., 2016; Behera et al., 2019) that the PBS is affected by the PAGS which, in turn, depends mainly on the temperature and time of austenitization. Additionally, the subsequent cooling rate can affect the final microstructure. For instance, higher cooling rates suppress atomic diffusion leading to smaller ferritic grains and increasing the dislocation density in the material (Ghosh et al., 2005; Das et al., 2003). Therefore, the PBS refinement in the R2S1 and R3S1 specimens may be a consequence of their shorter austenitization time as well as their faster cooling rate about the S1 condition. More specifically, the average PBS in the R2S1 sample is bigger than in the R3S1 condition. This difference in PBS between these patented samples was assumed to be an effect of the different austenitization temperatures (1100 and 950 °C) since they have the same austenitization time (390 s).

Also, the smallest average PBS, 5.9 μm ± 0.4 μm, was observed in the sample R4S2 which underwent prior cold-rolling deformation (30% of reduction) before the PT. In Fig. 2 **(j)** and **2 (k)**, it is possible to observe in the R4S1 sample shear bands mainly constituted by LABs (2–5°) and MABs (5–15°), as indicated by black arrows. The local lattice distortions with misorientation $< 15°$ (LABs and MABs) indicate areas with a concentration of geometrically necessary dislocations (GNDs) (Wright et al., 2011). In contrast to the S1 sample, the 30% cold-worked sample (R4S1) presented the highest total length of LABs (2.0 $\mu m/\mu m^2$) and MABs (0.7 $\mu m/\mu m^2$) per area. Therefore, R4S1 has a greater number of sites for austenite nucleation than S1 during PT. This circumstance leads to the earlier meeting between the R4S1′s austenitic grains still in small sizes. As a consequence, the smaller.

austenitic grains may act as a barrier against each other, preventing them to grow excessively (Humphreys et al., 2017). As a result, a refined prior austenitic grain may provide smaller pearlitic blocks as previously mentioned. Moreover, the R4S2 microtexture in Fig. 2 **(l)** did not exhibit the cube component, instead, it reveals a weak $\{001\}< 110 >$ orientation and a sharp component around the $\{554\}< 225 >$ and $\{111\}< 112 >$ orientations. This result indicates that the cube component is unstable during the cold-rolling process and initially, it may be rotated into $\{001\}< 110 >$ (Kestens and Jacobs, 2008). Subsequently, intermediary rotations along RD//$< 110 >$ components ($\{114\}<110 >$, $\{113\}<110 >$,$\{112\}<110 >$, $\{223\}<110 >$ or $\{445\}< 110 >$) are also able to occur during the cold-rolling deformation, followed by rotations toward more stable components such as $\{554\}< 225 >$ to $\{111\}< 112 >$ to $\{111\}< 110 >$ (Tóth et al., 1990). Furthermore, the total length of HABs of the S1, R2S1, R3S1, and R4S2 conditions in Fig. 3 **(b)** shows an expected inversely proportional relationship with the measured PBS in Fig. 3 **(a)**. However, a smooth divergence in this trend was found in the R3S1 condition in contrast to the R2S1. This exception should be due to the huge standard deviation in the R3S1′s PBS.

Moreover, it is worth noting that all the three samples just after the PT (R2S1, R3S1, and R4S2) in Fig. 2 **(f)**, **2 (i)**, and **2 (o)**, have an identical $\{011\}< 100 >$ (Goss) component, and their maximum microtexture intensities decreased in comparison to their prior process step (S1 or R4S1). Mandal et al. (2016) revealed that an increase in cooling rate from the austenitic region affects the variant selection during γ/α transformation that strengthens the ferritic Goss texture. Moreover, it is well known from the literature (Waterschoot et al., 2002) that the ferritic Goss component is strong evidence of recrystallized austenite with $\{001\}< 100 > \gamma$ (cube) texture. Therefore, it is reasonable to consider that during the PT's austenitization the new austenitic grains were likely nucleated with cube orientation, and then, the faster cooling rate could have assisted the development of ferritic grains with Goss orientation. Additionally, the most stable component detected in R4S1, the $\{111\}< 112 >$ orientation, is still seen after PT in the R4S2 condition, however, with a weaker intensity. In particular, R2S1 also exhibited a significant $\{011\}< 111 > \alpha$ component. Javaheri et al. (2021) reported that the development of $\{011\}< 111 > \alpha$ is related to shear strain. It reflects that the higher undercooling (ΔT) applied in the R2S1 condition, from 1100° to 550°C, may have resulted in some lattice shear strain. Regarding the cooling effect under the ferritic matrix, Fig. 3 **(b)** shows an increase in the total length of LABs and MABs in the following sequence: S1 < R3S1 < R4S2 < R2S1. It may support the assumption that the higher undercooling in R2S1 resulted in more distortion/strain in the ferritic lattice. Moreover, there is a huge difference in the total length of LABs and MABs between the R3S1 and R4S2 samples, which may be a consequence of their distinct thickness of 4.4 mm and 3 mm, respectively. It means that the quenching in bath salt from the same temperature (950 °C) should have more influence on the

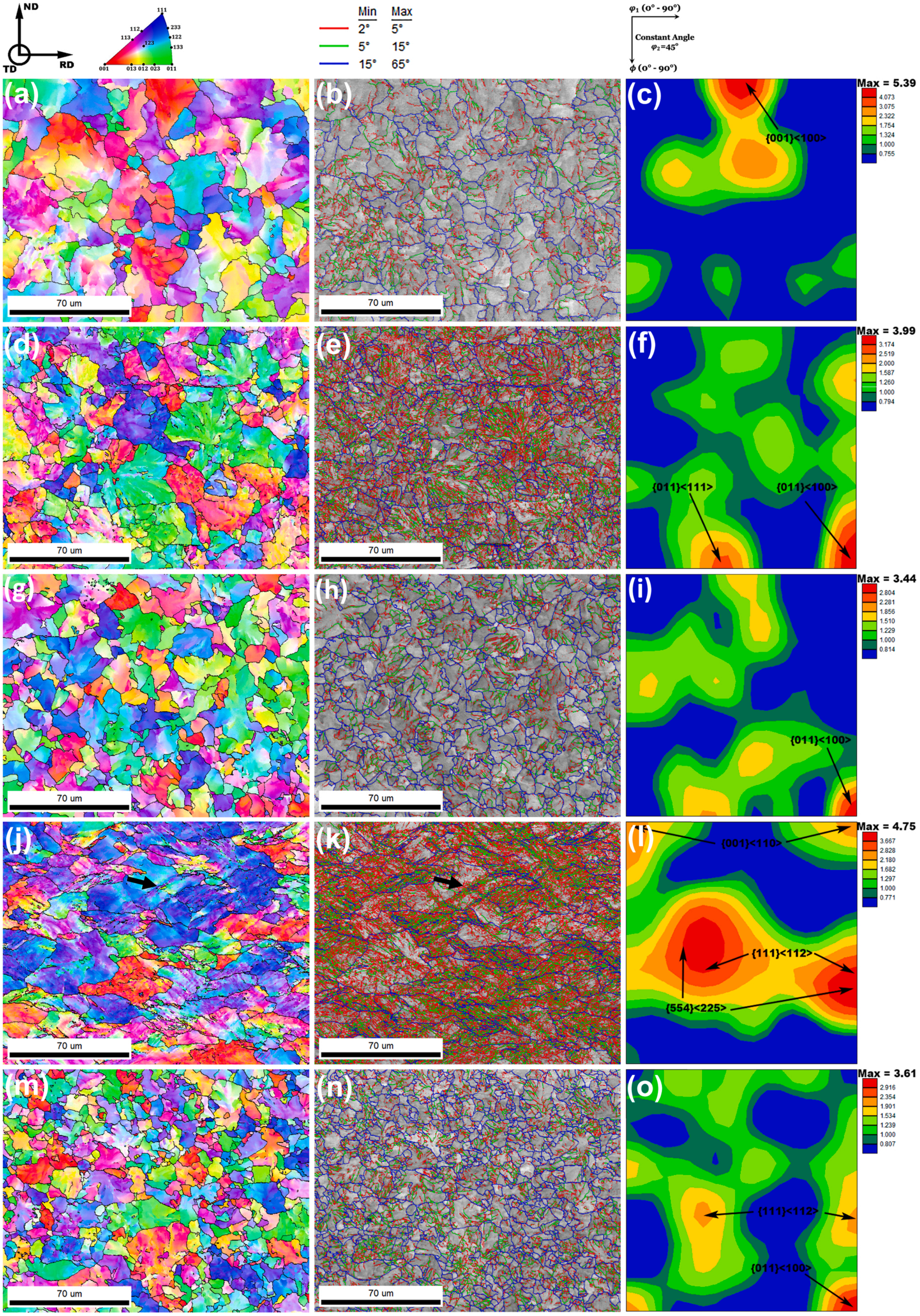

Fig. 2. Color-coded inverse pole figure (IPF) map, grain boundary distribution map, and orientation distribution function (ODF) at ϕ2 = 45°, respectively, for the samples: (a)(b)(c) S1, (d)(e)(f) R2S1, (g)(h)(i) R3S1, (j)(k)(l) R4S1 and (m)(n)(o) R4S2. The black arrows in the color-coded IPF and grain boundary distribution maps of the R4S1 sample point out a shear band.

Table 2
Summary of the main microtexture components found in the ODFs shown in Fig. 2 for the five samples before 65% cold-rolling reduction.

Sample's name	Main components	Intensity (mrd)
S1	{001} < 100 >	5.39
R2S1	{011} < 100 >	3.99
	{011} < 111 >	2.52
R3S1	{011} < 100 >	3.44
R4S1	{111} < 112 >	4.68
	{554} < 225 >	4.68
R4S2	{011} < 100 >	3.61
	{111} < 112 >	2.13

center of the thinner sample (R4S2) in comparison to the thicker one (R3S1). Likewise, this low quenching efficiency in the central region of the R3S1 sample may explain its larger standard deviation in the PBS which may be assumed as an indicator of a less homogeneous microstructure.

Furthermore, Fig. 4 shows IPF maps and their respective SEM images from the central region of each IPF map presented in Fig. 2. In Fig. 4 **(j), 4 (k),** and **4 (l)**, it is possible to confirm shear bands in the sample as indicated by red arrows. Also, Fig. 5 displays a summary of the IS, colony size, and microhardness measured in the four studied scenarios (S1, R2S1, R3S1, and R4S2) before the total 65% of cold-reduction. In general, it is possible to realize that, in comparison to the S1, the PT employment refined the IS and colony sizes as well as increased the microhardness. This increment in microhardness can be justified by the Hall-Petch relationship (Ohba et al., 2007). Specifically, R2S1 presented the greatest microstructural refinement and homogenization (shorter standard deviation) likely due to the highest undercooling ($\Delta T_{R2S1} = 550\ ^{\circ}C$) introduced in this condition. Otherwise, the IS, colony size, and standard deviation were larger in the R3S1 sample. In this context, the PT was performed under the same sample thickness (4.4 mm) and bath salt temperature (550 °C) in the R2S1 and R3S1 conditions,

while the undercooling ($\Delta T_{R2S1} = 550\ ^{\circ}C$ and $\Delta T_{R3S1} = 400\ ^{\circ}C$) and austenitization temperature ($AT_{R2S1} = 1100\ ^{\circ}C$ and $AT_{R3S1} = 950\ ^{\circ}C$) were the different parameters between them. Aranda et al. (2014) suggested that the ΔT may influence the diffusion distance for the solute transport, which is the main mechanism to control the interlamellar spacing. Moreover, the IS refinement as a result of an increase in the austenitization temperature was also reported by Dey et al. (2018). They described that carbon diffusion is more pronounced at higher austenitization temperatures, so a more homogenized distribution of carbon is expected in the austenitic matrix. Therefore, this event retards the formation of cementite plates, decreasing the IS. Otherwise, it can be seen in the R4S2 sample, that the low microstructural refinement and homogenization (reduction in the standard deviation) efficiency caused by a shorter ΔT or lower austenitization temperature can be compensated by the thickness reduction.

Regarding the formation of grain boundary of ferrite (GB-α) in the studied pearlitic steel, Fig. 6 displays many GB-α regions pointed out by white arrows. The measured volume fraction of GB-α increased from 0.42% in the S1 condition to 1.63%, 1.76%, and 2.84%, respectively, in the patented conditions R2S1, R3S2, and R4S2. Miyamoto et al. (2016) revealed that the amount of GB-α increased with the decrease of the prior austenitic grain boundary and γ/α transformation temperature. In this context, the authors described that the prior austenitic grain boundaries are sites for GB-α nucleation and GB-α growth is faster at lower γ/α transformation temperatures due to the inhibition of manganese partitioning. Thus, the resultant amount of GB-α can be explained by the austenitization condition and the sort of cooling applied in each of the four evaluated scenarios. Therefore, as the S1 austenitization condition has in sum the longest total hold time (960 s), it suggests that S1 has the biggest resultant PAGS. Another point is that S1 underwent the smallest cooling rate, which means it has the highest γ/α transformation temperature in which the mechanism of manganese partitioning may be able to occur, slugging the GB-α growth. So, these phenomena should justify the smallest volume fraction of GB-α found in the S1 condition as shown in Fig. 6 **(a)**. Regarding the patented specimens and also their austenitization parameters, as previously mentioned, they have the trend of decreasing their PAGS in the following sequence R2S1 > R3S2 > R4S2, which may justify their different amount of GB-α. As evidence, it is possible to realize that the GB-α seems to nucleate essentially in the boundaries of a bigger PAGS in Fig. 6 **(b)** and smaller PAGS in Fig. 6 **(d)**. Furthermore, probably due to the higher ΔT, Widmanstatten ferrite was only found in the R2S1 sample, as pointed out through thin white arrows in Fig. 6 **(b)**.

3.2. *65% cold-rolled samples*

This section centers attention on the four 65% cold-rolled samples (R1S1, R2S2, R3S2, and R4S3) produced from distinct lab-simulated process routes as illustrated in Fig. 1**(a)**. Fig. 7 exhibits SEM images and IPF maps with their respective ODFs of the R1S1, R2S2, R3S2, and R4S3 samples. After the 65% cold-rolling deformation, it is possible to observe that the pearlitic colonies, the GB-α, and the pearlitic blocks tend to be stretched in the rolling direction, as shown in Fig. 7. Specifically, it is possible to see in Fig. 7 **(a)**, **7 (d)**, **7 (e)**, and **7 (g)** bent and broken cementite lamellae due to shear bands (indicated by smaller white arrows) or the hard initial orientation of the cementite lamellae about the rolling direction (indicated by bigger white arrows).

In addition, it is worth realizing that the thickness and length of the

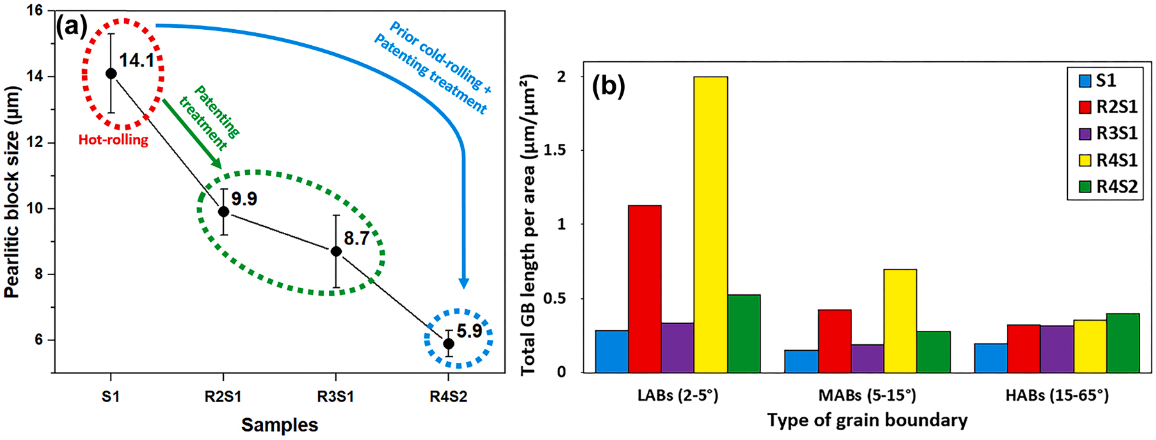

Fig. 3. (a) Pearlitic block size average of the hot-rolled (S1) and the patenting treated (R2S1, R3S1, and R4S2) samples, and (b) distribution of grain boundary type per area regarding the samples S1, R2S1, R3S1, R4S1, and R4S2.

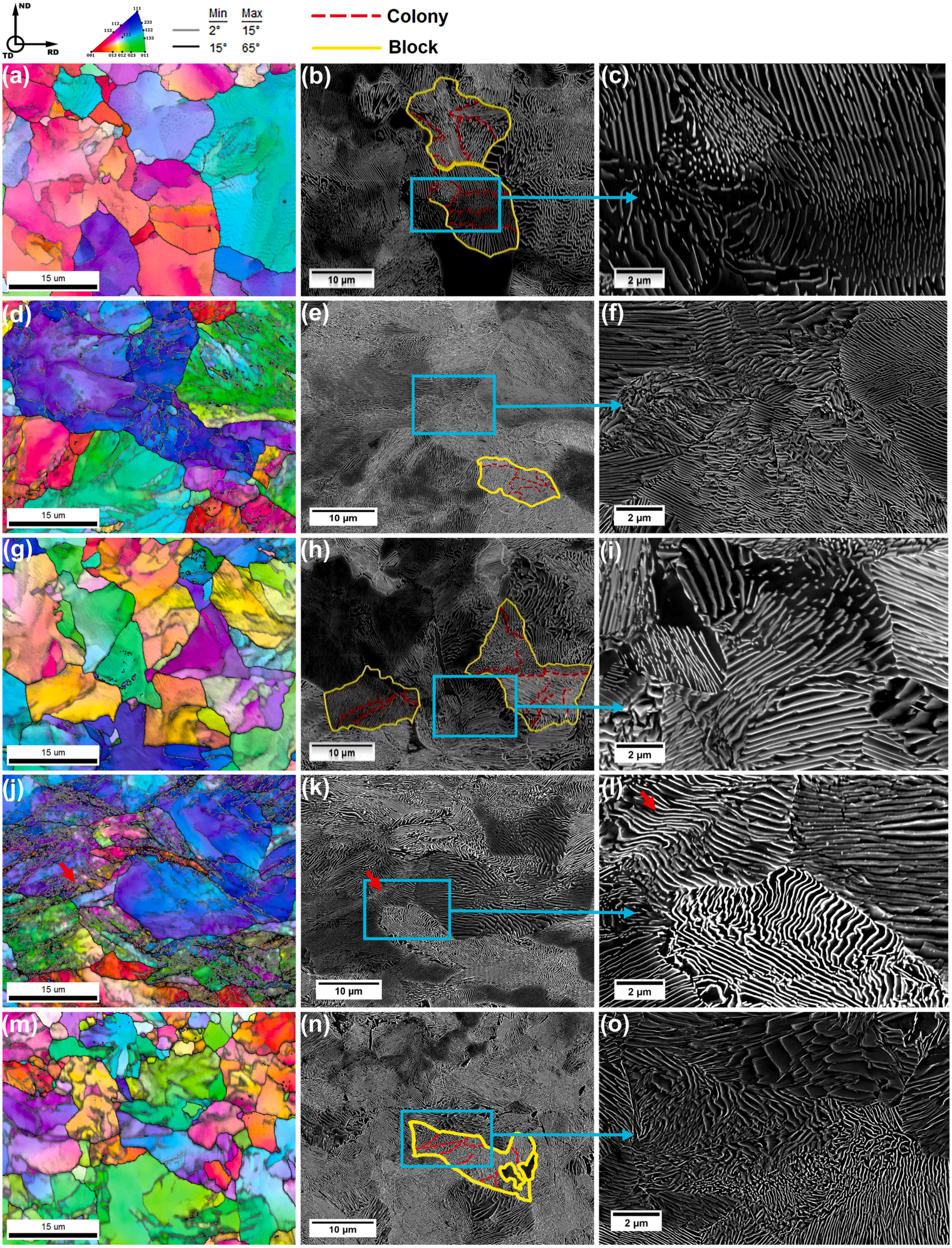

Fig. 4. Color-coded inverse pole figure (IPF) map, Scanning electron microscope (SEM) Secondary electrons (SE) image of the IPF map area and SEM SE image in higher magnification, respectively, of (a)(b)(c) sample S1, (d)(e)(f) sample R2S1, (g)(h)(i) sample R3S1, (j)(k)(l) sample R4S1 (the red arrows indicate a shear band) and (m)(n)(o) sample R4S2.

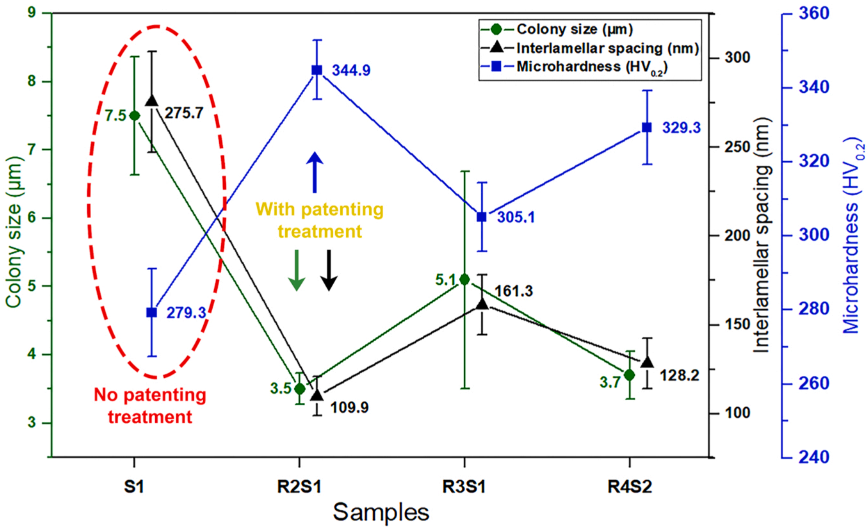

Fig. 5. Values of interlamellar spacing, microhardness, and colony size for the S1, R2S1, R3S1, and R4S2 processed conditions.

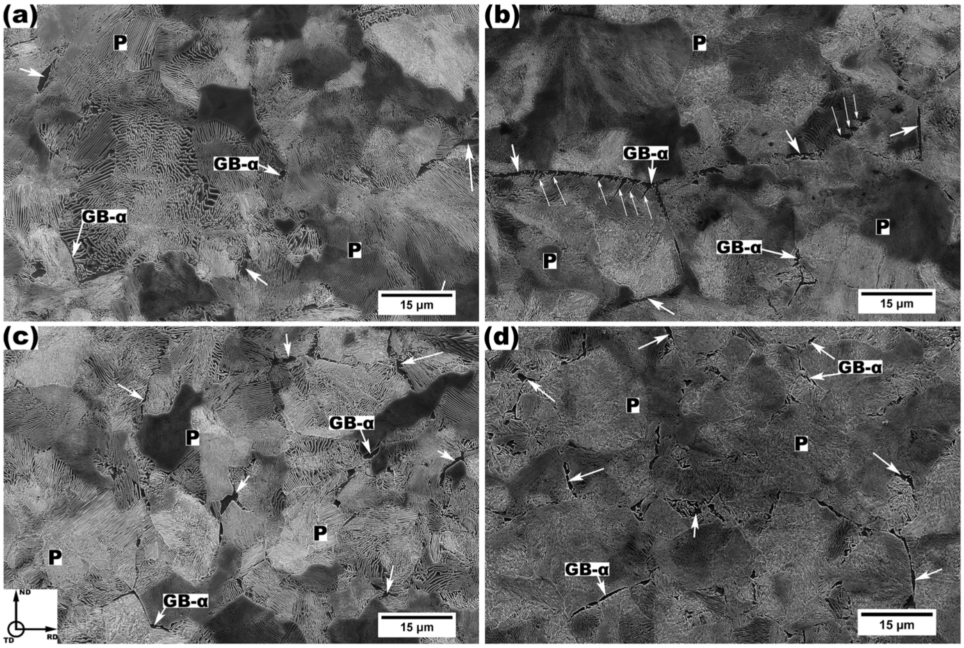

Fig. 6. SEM SE image of GB-α (indicated by the big white arrows) and pearlite distribution in the matrix of the (a) sample S1, (b) sample R2S1 (the smaller white arrows indicate Widmanstatten ferrite), (c) sample R3S2, and (d) sample R4S2.

stretched pearlitic blocks are proportional.

to their size before the cold deformation, which means that the initial condition with the biggest undeformed pearlitic blocks resulted in the longest stretched ones after deformation (for example, see Fig. 7 **(b)**) and so on. In this context, the pearlitic blocks seem to have different trends of deformation. The bigger pearlitic blocks with larger stretched areas presented a greater density of shear bands, such as in the samples R1S1 (Fig. 7 **(b)**) and R2S2 (Fig. 7 **(e)**) which is consistent with a previous investigation (Jazaeri and Humphreys, 2004). This phenomenon can be associated with a lower strain-rate sensitivity (m) in the conditions of pearlitic steel with big pearlitic blocks. In this regard, Figueiredo and Langdon (2022)) demonstrated in their model that strain-rate sensitivity has an inversely proportional relationship with the grain size in BCC metals. Also, the authors reported that lower flow stresses are required to continue deforming plastically the coarse-grained materials with low strain-rate sensitivity. Additionally, Yan et al. (2021) described that low strain-rate sensitivities can lead to, eventually, strain localization in the material. Therefore, it may imply that the big pearlitic blocks are more susceptible to the development of shear bands in comparison to the smaller ones under the same reduction per pass, rolling speed, and total reduction during the cold rolling process. Moreover, it is also reasonable to consider that the lattice rotations during deformation occur less distributed inside the big pearlitic blocks due to the development of many local deformations (shear bands). It suggests that this mechanism may slice the block into different sections that can slightly slide over each other as deformation occurs. As consequence, a large pearlitic block may be stretched into the rolling direction by undistributed lattice rotation and predominantly local deformation (shear bands).

Another relevant indicator of lattice rotation is microtexture development. From the ODFs in Fig. 7 **(c)**, **(f)**, **(i)**, and **(l)** the main cold-rolling components found were in the α (RD//<110 >) and γ (ND//

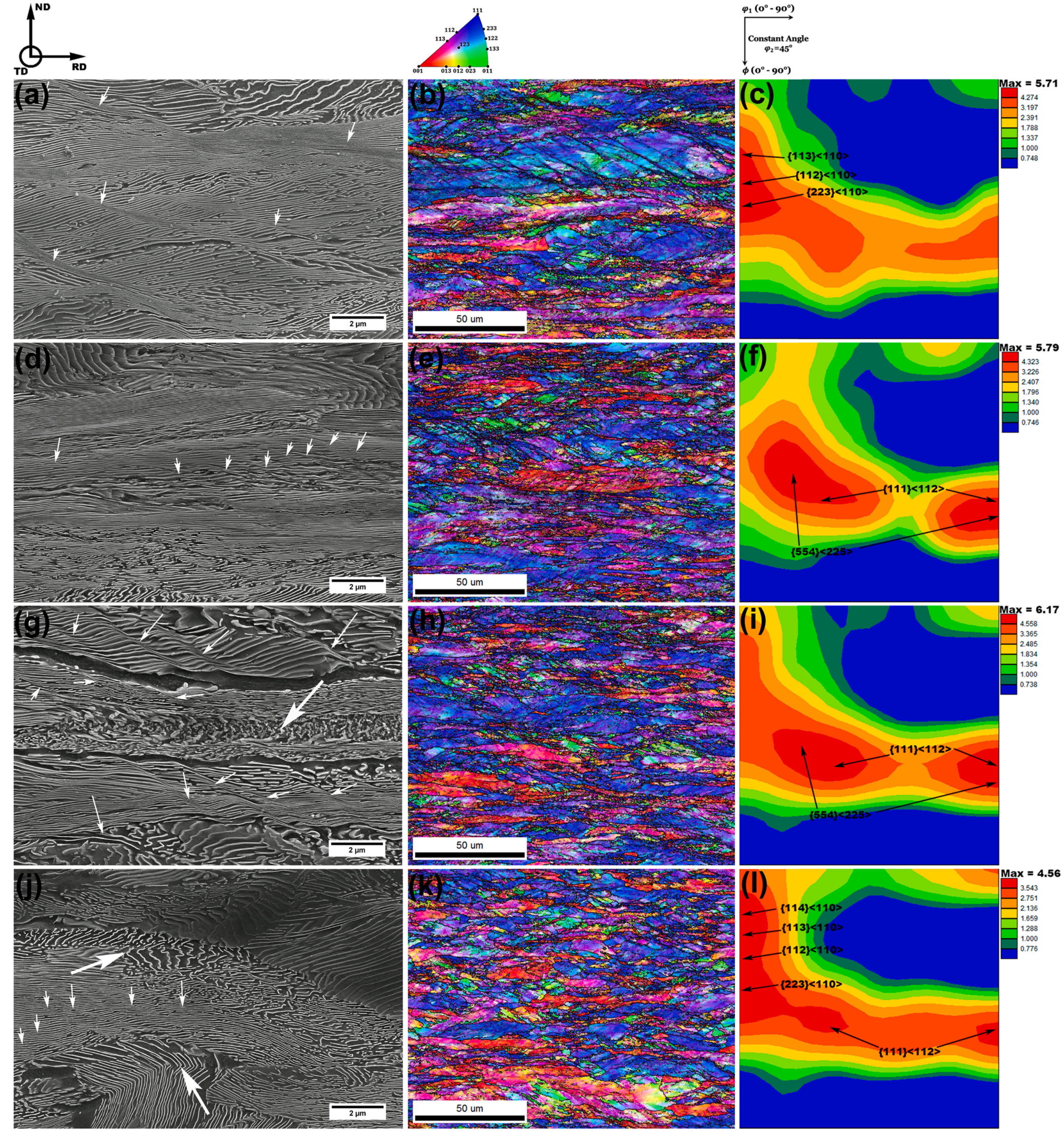

Fig. 7. SEM SE image, color-coded IPF map and ODF at ϕ2 = 45°, respectively for each cold-rolled samples: (a)(b)(c) R1S1, (d)(e)(f) R2S2, (g)(h)(i) R3S2 and (j)(k)(l) R4S3. In the SE images, small white arrows indicate bent and broken cementite lamellae caused by shear bands, while big white arrows point out bent and broken cementite lamellae due to their hard initial orientation with the rolling direction.

<111 >) fibers. However, considering just the samples R1S1, R2S2, and R3S2, it can be seen that the intensity of the ND//< 111 > fiber, mainly represented by {111}< 112 > component or dark blue pearlitic blocks, increases as the PBS before the cold-forming decreases. This relationship is evidenced in Fig. 8 **(a)**. However, in Fig. 8 **(a)**, the R4S3 condition was indicated as a special case because its smallest PBS before cold-forming did not result in the biggest {111}< 112 > intensity. It can be explained due to the application of the PT (ND//<111 > fiber weakener) after the first 30% of cold reduction. However, after just an additional 35% of cold thickness reduction, the R4S3 condition possessed as one of its main components the {111}< 112 > orientation, which was even bigger than in the R1S1 condition. Therefore, the special case condition (R4S3) also provides a noticeable effect of the PBS on the crystallographic lattice rotation during the cold-rolling process. So, the ODFs' microtexture in Fig. 7 may confirm that the smaller pearlitic blocks which have greater restraint limits (block boundaries) have more effective lattice rotation in comparison to the bigger pearlitic blocks. Therefore, it suggests that the PT application before cold-rolling can have a straight influence on the

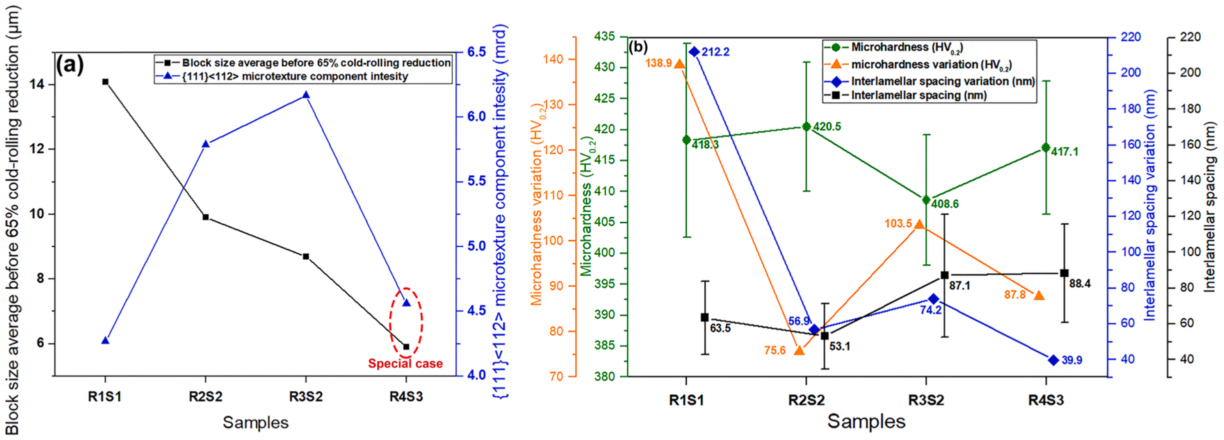

Fig. 8. (a) Pearlitic block size before 65% cold-rolling reduction against its {111}< 112 > microtexture component intensity after 65% cold-rolling reduction for the R1S1, R2S2, R3S2, and R4S3 samples (the red dashed circle and the special case reference meaning a different cold-rolling process in the R4S3 condition) and (b) Values of microhardness, interlamellar spacing, and their variation concerning one condition before in the process route of the R1S1, R2S2, R3S2, and R4S3 cold-rolled samples.

cold-rolling microtexture by modifying the initial PBS.

Furthermore, Fig. 8 **(b)** summarizes the IS and microhardness obtained from the four investigated 65% cold-rolled samples (R1S1, R2S2, R3S2, and R4S3) and their respective variation concerning the sample one position backward in their respective manufacture route sequence (S1, R2S1, R3S1, and R4S2, respectively). The IS and microhardness variation reveals that all the samples underwent an IS reduction and microhardness increase as a result of the cold-rolling deformation. In addition to this, it can be seen that the magnitude of the increase in microhardness (orange plot in Fig. 8 **(b)**) followed a close trend to the IS refinement (blue plot in Fig. 8 **(b)**). In this regard, the cementite lamellae are barriers to the dislocation slip in the ferrite phase that can generate dislocation pile-ups at the lamellae interface (Eshelby et al., 1951). So, the corresponding IS/microhardness variation can be explained via the Hall-Petch relationship (Ohba et al., 2007). Moreover, dislocations formed at the cementite/ferrite interface can drag carbon atoms from the cementite into the ferrite matrix resulting in a hardening contribution through a ferrite solid solution (Li et al., 2011). However, the IS and microhardness varied differently for the same degree of cold-rolling reduction (65%). In this way, the biggest IS change was noticed between S1 (hot-rolled) and R1S1 (65% cold-rolled) conditions. This high IS refinement capacity may be attributed to the higher elongation undergone by the big blocks in the R1S1 sample during the cold-forming process. Also, Li et al. (2011) reported that pearlites with coarse IS are the preferable source for dislocation nucleation due to their lower critical stress. It means that coarse microstructure pearlites may undergo higher strain than the thinner ones under the same degree of cold reduction. So, the initial tick IS colonies in sample S1 with lamellae soft orientated to the rolling direction may be drastically refined due to their superior capacity for stretching and undergoing strain. Moreover, between the four 65% cold-rolling reduced conditions, the thinnest IS average was achieved in the sample R2S2. In this case, it should be a result of the combined contribution of the already refined IS before plastic deformation in sample R2S1 and its second-largest PBS with relevant stretching performance. Regarding the same assumption, although the samples R3S2 and R4S3 (with the smaller PBS) presented IS reduction, they did not reach great thinning efficiency likely due to their poor lengthening ability.

In addition, the microhardness values (green plot in Fig. 8 **(b)**) of the four 65% cold-rolled samples (R1S1, R2S2, R3S2, and R4S3) were considered indistinguishable from each other, mainly because their standard deviation involved an extensive correspondent range of fluctuation between them. Thus, it is plausive to consider that the different IS magnitudes generated after the same degree of cold-rolling deformation in the four investigated conditions were not enough to affect individually their microhardness. Instead, as reported by several researchers (Tagashira et al., 2000; Guo et al., 2014; Zhang et al., 2007), the variation in the amount of plastic deformation may be the dominant parameter for producing significant IS variance and consequently, mechanical properties divergence after the cold-forming process. Finally, the most distinct microhardness average (408.58 HV) and the highest standard deviation (± 16.16) were observed in the R3S2 (which had the smaller microhardness) and R1S1 conditions, respectively. These discrepancies may be a consequence of inhomogeneous microstructure resulting from no PT adoption (S1 condition) or low efficiency of PT employment (R3S1 condition).

3.3. *Stress-relieved samples after 65% cold-rolling reduction in route 3*

In the current work, only the stress-relieved condition at 700 °C for 60 s in route 3 presented cracks during the bending experiments (see Fig. 1**(a)**). Regarding the route 3 pathway, this topic focuses on investigating the microstructural effects caused by the stress relief treatments applied just before the three-point bending procedure in the R3400 (400 °C for 60 s) and R3700 (700 °C for 60 s) samples.

Fig. 9 exhibits the resultant pearlitic microstructures after stress relief treatment at 400 °C (R3400) and 700 °C (R3700) for 60 s of holding time in both. The lamellar morphology was the dominant sort of pearlite found in the R3400 condition as shown in Fig. 9 **(a)**, which means that this microstructure is similar to the 65% cold-rolled state (R3S2). Also, the R3400′s microhardness, 409 ± 7 HV, did not reveal an appreciable difference about R3S2 (407 ± 9 HV). Therefore, it is reasonable to suggest that the thermal treatment at 400 °C for 60 s was not enough to strain-relief the prior cold-deformed state (R3S2). In contrast, the short holding time (60 s) at 700 °C was enough to start the process of cementite spheroidization as shown in Fig. 9 **(b)**. As a consequence, the microhardness dropped to 358 ± 6 HV. The regular process of cementite spheroidization is reported to take many hours (Montana et al., 2022). So, the faster spheroidization event observed in the R3700 condition may be attributed to the introduction of subgrains to the ferrite and cementite phases during the prior plastic deformation process (Montana et al., 2022; Lupton and Warrington, 1972). However, it is worth noticing that this cementite spheroidization was not homogeneous. In this regard, it is possible to identify in Fig. 9 **(b)** three different cementite morphology: disconnected but still elongated cementite (red arrows), partially spheroidized cementite (yellow arrows), and completely spheroidized cementite (orange arrows). This outcome may be a consequence of the heterogeneous microstructure produced from both;

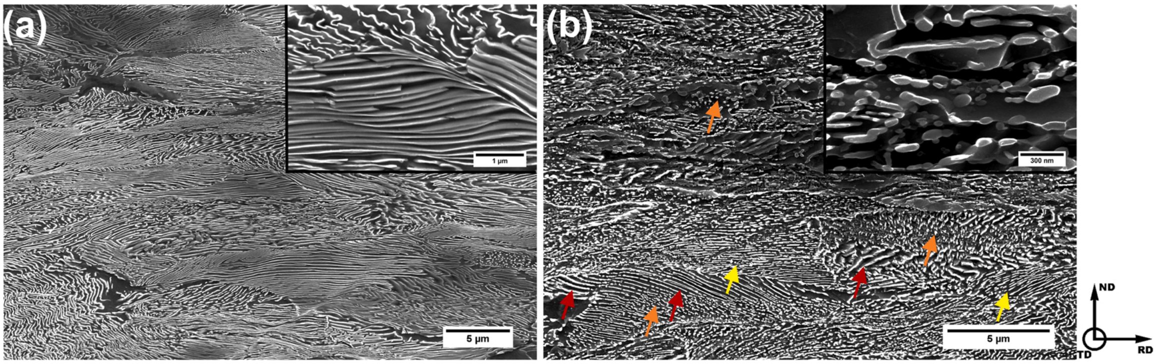

Fig. 9. SEM SE image of the 65% cold-rolled pearlitic steel (R3S2) after stress relief treatment at (a) 400 °C during 60 s (R3400) and (b) 700 °C during 60 s (R3700) (The red arrows point out disconnected and elongated cementite, the yellow arrows indicate partially spheroidized cementite, and the orange arrows indicate the completely spheroidized cementite).

irregular PT application (huge variation of IS) and cold-rolling process (undistributed strains). Concerning the irregularities and discontinuities even within the same pearlite, it is pointed out from the literature (Montana et al., 2022; Zhao et al., 2022) that lamellae cementite from thinner IS regions in pearlites are easier to dissolve into the matrix during thermal treatments, and localized strains in pearlites, such as shear bands, are regions prone to cementite spheroidization. Moreover, after a short annealing time at 700 °C of 70% cold-rolled pearlitic steel, Furuhara et al. (2005) described that spheroidization cementite starts in large misorientation regions in the ferritic matrix where lamellae are heavily deformed, such as in irregular bent lamellae and shear bands. Also, the authors found non-spheroidized cementite from coarse lamellae regions. They still reported disconnected cementite but still elongated from fine cementite lamellae areas with no local strain. In agreement with the aforementioned investigation, Fig. 10 shows that spheroidization cementite mainly occurs in the shear bands (indicated by white arrows) followed by irregular bent lamellae zone (pointed out by an orange arrow).

Furthermore, Fig. 11 presents IPF maps for the two evaluated stress-relieved conditions (R3400 and R3700) and their respective grain boundary distributions, ODFs, and Taylor factor maps. It is interesting to note that the ferritic blocks in the IPF maps are still elongated to the rolling direction in both investigated circumstances. However, as indicated by a white dashed circle, Fig. 11**(b)** presents many small randomly orientated and equiaxed ferritic grains inside a blue block, which are aligned to each other and seem to follow the same direction as the previously observed shear bands. In addition to this, in Fig. 11 **(e)** the stress-relieved condition at 700 °C presented a lower amount of LABs summed to MABs and a greater amount of HABs in comparison to the stress-relieved state at 400 °C. Regarding this, a high density of HABs is concentrated in the region where the small equiaxed ferritic grains were found, as shown in Fig. 11 **(d)**. It means that these new grains are surrounded by high-angle boundaries. Conversely, the R3400 sample displayed a resultant distribution of HABs more homogeneously spread throughout the matrix. Moreover, regarding {111}< 112 > component formed during the prior 65% cold-rolled reduction (R3S2), the ODFs presented in Fig. 11 **(f)** and **11 (g)** exhibited a reduction of {111}< 112 > intensity only for the R3700 condition.

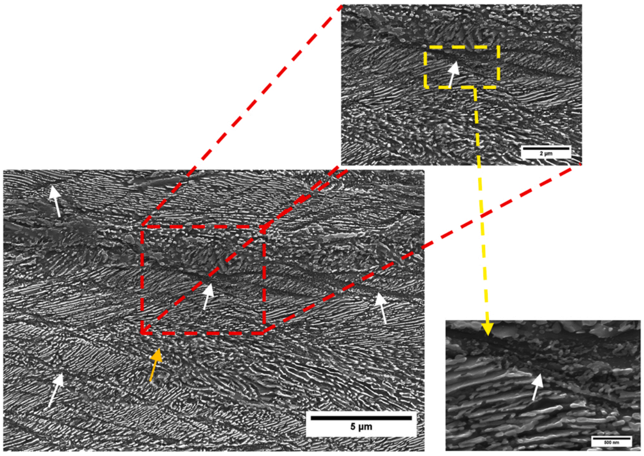

Fig. 10. SEM SE images indicate cementite spheroidization in the shear bands (pointing out by white arrows) and in the irregular bent cementite zone (pointing out by an orange arrow) after stress relief treatment at 700 °C for 60 s (R3700 condition).

In this context, it may be considered that the small equiaxed grains found in R3700 seem to be formed via recrystallization. Besides, it is known from the literature (Furuhara et al., 2005; Leão et al., 2022) that the {111}< 112 > orientation originated via plastic deformation is the component that contains the highest stored energy, and the shear bands are regions with high misorientation. Based on this information, it is plausive to assume that the preferential site for new recrystallized grains should be in the shear bands inside the {111}< 112 > orientated blocks (dark blue ones), which can explain the arrangement of how the set of the small ferritic grains are displayed in Fig. 11 **(b)**. As a consequence of this mechanism, the intensity of {111}< 112 > component should smoothly decrease as shown in Fig. 11 **(g)**. However, it can still be seen that the fast thermal treatment did not eliminate all the {111}< 112 > blue grains with shear strains as pointed out by white arrows in Fig. 11 **(b)**. Concerning that cementite spheroidization was intensively developed mainly in the shear bands (see Fig. 10), the small recrystallized ferritic grains hardly grow due to the pinning effect of the distributed cementite particles in these regions (Umar et al., 2021). This can make it difficult for high-angle boundaries to migrate. Moreover, the reduction of grain boundaries with low/medium misorientation (<=15°) and the increase of HABs due to the nucleation of many small grains with low capacity of motion implies that the formation of the new grains happens basically via recovery. This event is known as continuous recrystallization (Haessner, 1978).

Also, Fig. 11 **(h)** and **11 (i)** display Taylor factor maps for both evaluated stress relief conditions. Taylor factor analysis can predict the ability of grains to undergo plastic deformation based on the crystallographic orientation distribution and active slip systems concerning the external loading direction (Liu et al., 2016). To clarify, slip plains' grains already aligned into the loading direction, easily slip when the resolved critical shear stress is achieved. These grains have low Taylor factor values and are represented by blue grains in the Taylor factor maps. There are also initially not aligned slip systems' grains, which can rotate to a suitable position where plastic deformation can occur. This type of grain possesses a moderate Taylor factor and is indicated in yellow or green color in the Taylor factor maps. Finally, the red and dark yellow

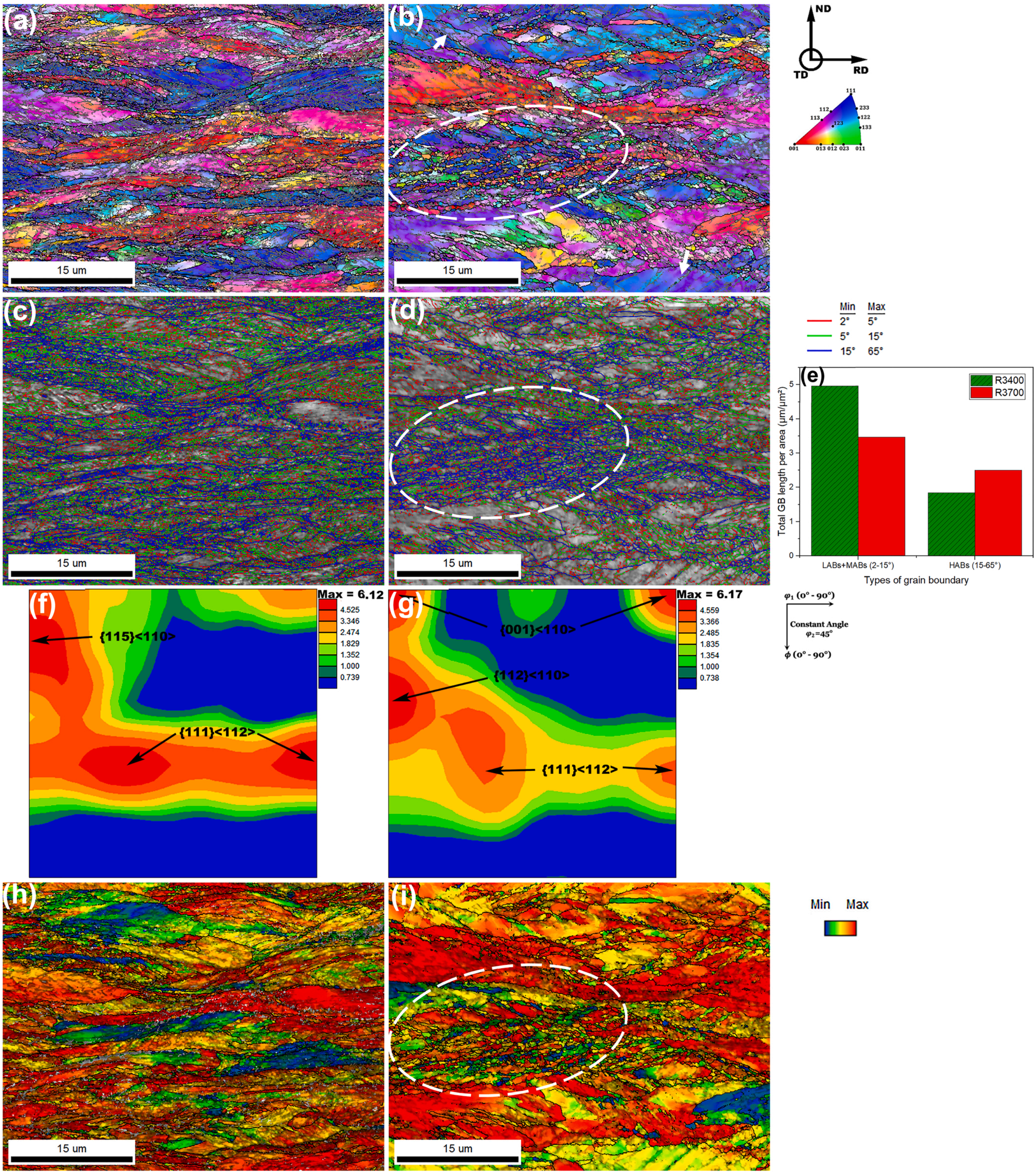

Fig. 11. Color-coded IPF map, grain boundary distribution map, distribution of grain boundary type per area, ODF at ϕ2 = 45° and Taylor factor map, respectively, of the (a)(c)(e)(f)(h) sample R3400 and (b)(d)(e)(g)(i) sample R3700. The dashed white circle indicates a region with recrystallized small grains.

grains with a high Taylor factor cannot rotate to provide the occurrence of plastic deformation. To summarize, the low Taylor factor means easy grain deformation, and conversely, the high Taylor factor represents grains with higher resistance to deforming. In this context, the Taylor factor map from the R3700 condition in Fig. 11 **(i)** shows that the region with small equiaxed grains (indicated by a white dashed circle) developed many local Taylor factor heterogeneities that are not possible to be observed in the R3400 (Fig. 11 **(h)**). In the region surrounded by a white dashed circle in Fig. 11 **(i)**, there are small blue and green grains oriented for easy slip, while those grains in dark yellow or red provide resistance for yielding. This mismatch of the Taylor factor between adjacent grains is prone to form intergranular cracks (Szpunar et al., 2015).

3.4. Mechanism of crack nucleation and propagation during bending test

This section aims attention to investigate cracks detected during bending experiments. These defects were found only in samples that came from the 65% cold-rolling process in route 3 followed by stress relief treatment at 700 °C for 60 s (see Fig. 1**(a)**). In this context, Figs. 12, 13, and 14 present three cracks found in three R3700crack samples after undergoing four consecutive and alternated three-point bending tests. In general, these cracks were found in the area close to the outer surface during the fourth bending sequence. Therefore, the cracked regions were under tensile at that testing moment, but this region was already submitted under the states of compression (first bending), tensile (second bending), and then, compression again (third bending). Recent works (Kapp et al., 2022; Arola et al., 2021) reported that the tensile region under bending conditions tends to form shear bands while the compressed one is kept smooth. Also, it is interesting to note that in some regions the microstructure was tilted and stretched into a specific direction that the cracks also tend to follow. This outcome was related to the round shape of the superior pin. It means that this new lengthened direction depends on which side of the superior pin the evaluated region is located. For instance, the areas shown in Figs. 12 and 13 were situated just below the left side of the superior pin, while Fig. 14 was below the right side. Moreover, it is not easy to observe the GB-α and the spheroidized cementite in the bent state, probably due to the severe plastic deformation associated with the repeated bending processes. For example, it is possible to recognize some stretched GB-α in Fig. 13 **(a)** and **14 (b)**, and some deformed regions with cementite partially spheroidized in Fig. 12 **(e)**, **12 (f)**, and **14 (d)**.

Fig. 12 **(a)** exhibits a crack with a length of 279.3 μm and an angle of ≈ 42.7° about the rolling direction. This crack presents many deviations.

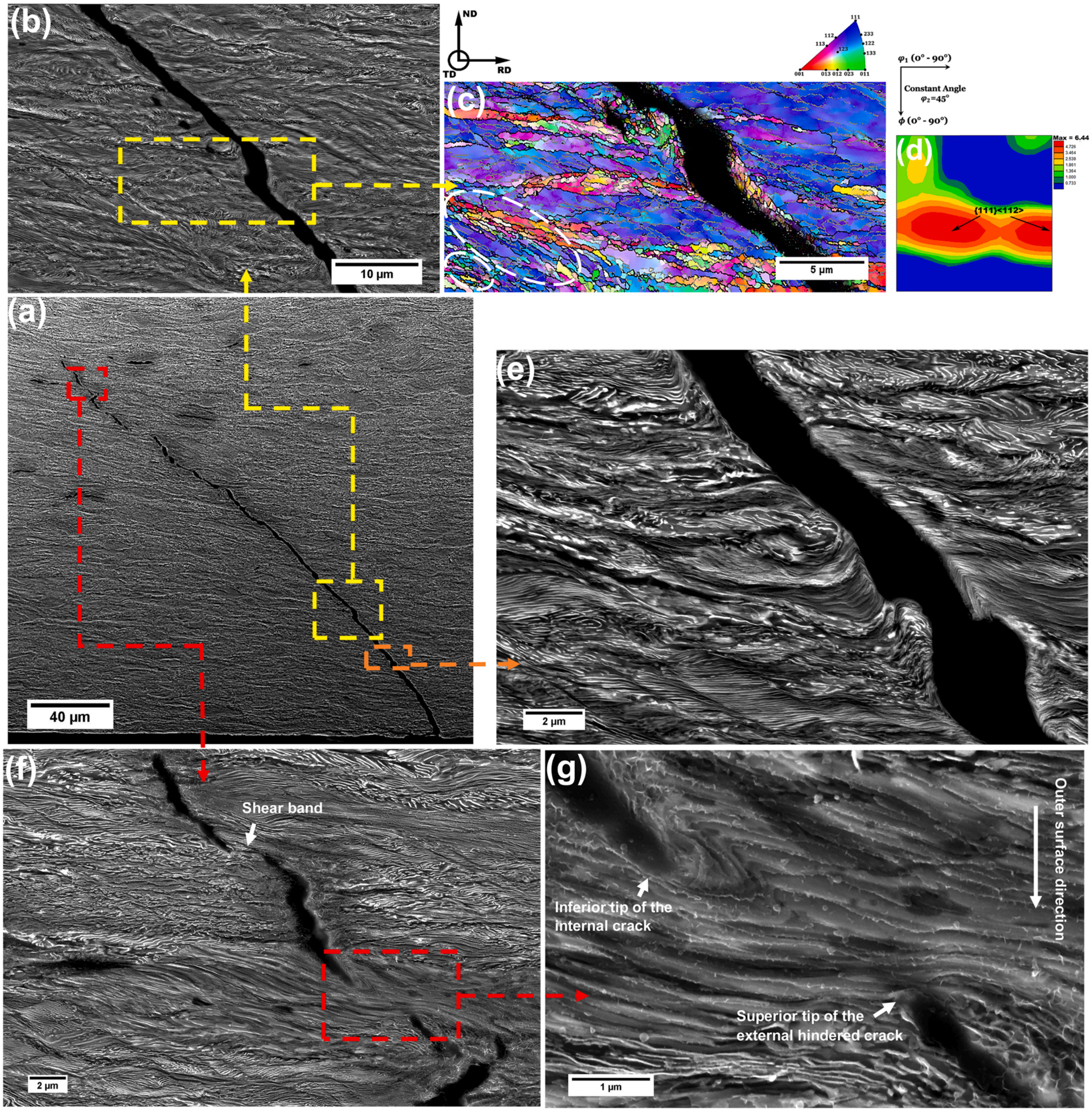

Fig. 12. Crack from the R3700crack sample condition in the tensile region of the fourth bending experiment and below the left side of the superior pin. (a) SEM SE image of the entire crack. (b) SEM SE image of a region with crack deviation and microcracks. (c) Color-coded IPF map of the region containing the crack deviation and one microcrack. The dashed white circles indicate small grains deformed in a direction almost parallel to the main crack and shear bands. (d) ODF at ϕ2 = 45° calculated from the IPF map in Fig. 12 (c). (e) SEM SE image of a smooth crack deviation. (f) SEM SE image of the region close to the crack tip. (g) SEM SE image from a crack's tip region showing the bending of a lamellar pearlite.

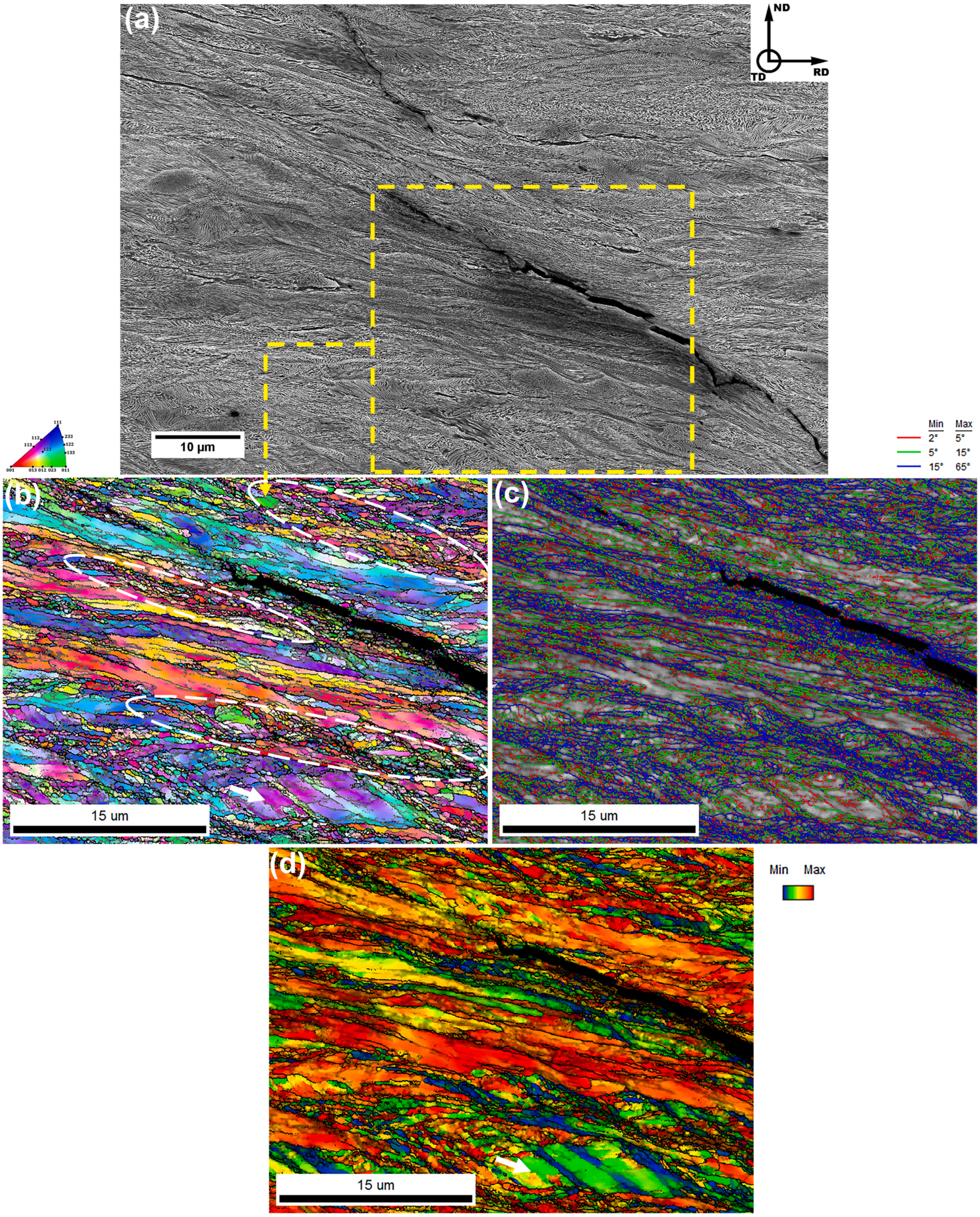

Fig. 13. Tip of a crack in the R3700crack sample condition, located below the left side of the superior pin in the tensile region after four alternating bending experiments. (a) SEM SE image. (b) Color-coded IPF map. The dashed white circles indicate regions of small grains deformed in a direction close to the crack propagation and shear bands. (c) Grain boundary distribution map. (d) Taylor factor map. The white arrow indicates a non-recrystallized and non-rotated grain with local shear strains.

One of these crack path divergences is shown in Fig. 12 **(b)**, where the pearlite colonies around the crack were not found much tilted, instead they presented shear bands. In this regard, the crack is aligned to those specific local strains. Moreover, in Fig. 12 **(b)** it is possible to notice three microcracks around the big one aligned to the inferior part of the main crack below the deviation. Additionally, it can be realized in the IPF map, in Fig. 12 **(c)**, that small grains are surrounding one of the microcracks and in some regions around the principal crack. Moreover, the crack is passing through a {111}< 112 > orientated grain as shown in Fig. 12 **(d)**. Supplementary, Fig. 12 **(e)** depicts another region in which the crack underwent a smooth path deviation. In this case, it is possible to detect quite bent cementite lamellae around the deviation region. The bent lamellar pearlite looked to be perpendicular to the direction of the crack propagation. Besides, the crack region just below the bent lamellae is round and thicker which seems that its prior propagation was hindered there. Another point is that the direction in which the lamellae were bent suggests that the superior crack reached the inferior one. Moreover, Fig. 12 **(f)** displays an area close to the tip of the evaluated crack. In this region, there are four main crack segments and four microcracks. In this context, it can be noticed that the pearlites around the two superior crack segments are partially spheroidized. In addition, it is possible to observe in the region between these two superior cracks they are connecting following a shear band, as indicated by a white arrow. This mechanism agreed with the model developed by Hu et al. (2010). The authors concluded that cracks initiated in distinct regions can be connected throughout shear bands during bending deformation. Otherwise, the inferior crack is deviating from a perpendicular and fully lamellar pearlite, however, the propagation of the inferior crack seems to be blocked. Then, in Fig. 12 **(g)**, it is visible that the crack segment located in the middle of Fig. 12 **(f)** is bending the pearlitic lamellae in the direction of the inferior microcrack. It seems to be the same phenomenon shown in Fig. 12 **(e)**. This crack propagation mechanism may be attributed to the gradient of tension during the bending experiment that should be zero in the middle thickness of the sample and increase to a maximum in the region close to the external surface (Kapp et al., 2022). So, this condition leads to a higher tensile stress in the inferior tip of the internal crack which promotes easier crack growth into the outer surface direction (see Fig. 12 **(e)**). In contrast, in the superior tip of the hindered external crack, the tensile stress is supposed to be smaller than in the rest of the crack which becomes difficult for the crack propagates through the transversal pearlitic lamellae.

In particular, the crack presented in Fig. 13 **(a)** has a length of 138.4 μm. In the region surrounding this crack, there are pearlites lengthened to ≈ 29.4° concerning the rolling direction. Saastamoinen et al. (2017) showed microcracks nucleating inside a shear band and following its direction during a bending test. Also, it is worth pointing out that a non-rotated grain, indicated by white arrows in Fig. 13 **(b)** and **13 (d)**, presented three local shear strains aligned near (≈33.8° about RD) to the direction of the stretched pearlites around the crack. Therefore, it is reasonable to accept that this local deformed microstructure may be part of a shear band caused by the bending deformation. In addition, it is possible to realize in Fig. 13 **(b)**, **13 (c)**, and **13 (d)** that the crack is propagating between the small high-angle boundary grains with a considerable mismatch of Taylor factors, which are also aligned close to the shear band direction. This result agrees with the microstructure described in the previous section (Fig. 11 **(b)** and **11 (i)**).

Additionally, Fig. 14 **(a)** exhibits another deep crack (542.4 μm) tilted ≈ 48.7° with the rolling direction. Fig. 14 **(b)** shows the tip of that crack which is also surrounded by deformed pearlites in the same direction of crack propagation. Moreover, the IPF map of this crack tip is shown in Fig. 14 **(c)**. It is possible to observe similarities in the propagation path to the prior cracks. In this case, the crack is passing between small grains inside the {111} oriented pearlitic block (blue) and follows the direction of the deformed blocks. It is clear to observe that the crack deviated from the {100} blocks in red color. Furthermore, Fig. 14 **(d)**

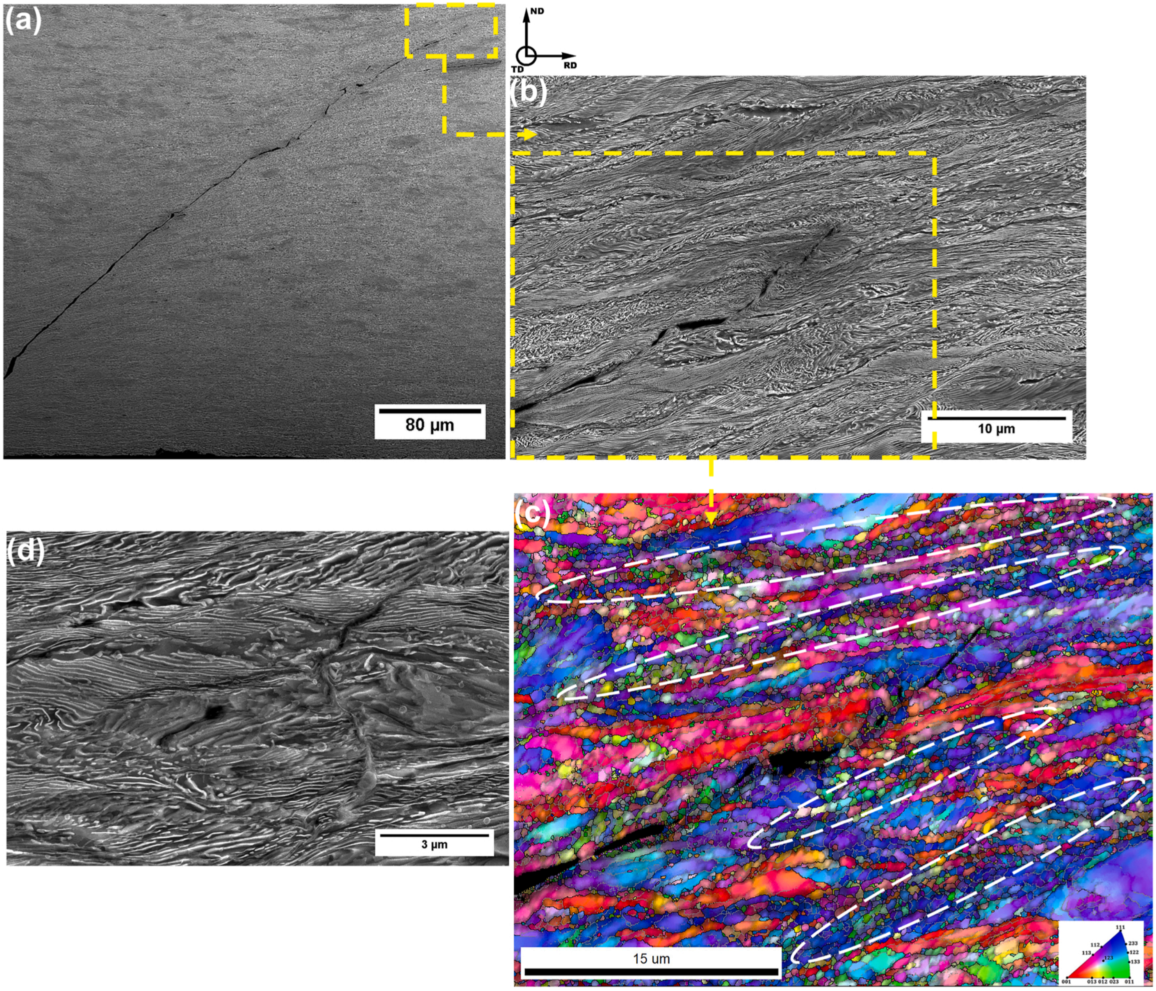

Fig. 14. Crack from the R3700crack sample condition in the tensile region of the fourth bending experiment and below the right side of the superior pin. (a) SEM SE image of the entire crack. (b) SEM SE image of the crack tip. (c) Color-coded IPF map of the crack tip. The dashed white circles indicate regions of small grains deformed in a direction close to the crack propagation. (d) Microcracks from an adjacent region around the main crack.

displays two microcracks found around the region of the main crack. One of them is propagated between the cementite/ferrite lamellar interface (decohesion) that probably originated from the round microcrack. While the second microcrack seems to be in pearlite with broken or partially spheroidized cementite. These cracks in Fig. 14 **(d)** are tilted and aligned in the same direction (≈33.4° with the rolling direction), which suggests that they are likely in a shear band orientation.

In summary, regarding the evidence discussed in the current section, it is reasonable to accept that shear band deformation can be induced via the three-point bending test in the sample's tensile region. However, part of the shear bands previously created during the cold-rolling process in the $\{111\}< 112 >$ blocks was replaced by many small recrystallized grains. In this way, every time this structure is submitted under a tensile condition, imposed throughout the successive bending deformation, new shear directions start to be developed in the material and the small grains inside the $\{111\}< 112 >$ blocks tend to align into the newly settled shear directions. This behavior can be seen in the regions indicated by white dashed circles in the IPFs maps presented in Fig. 12 **(c)**, **13(b)**, and **14 (c)**. Moreover, it is plausive to acknowledge that the small recrystallized grains inside the $\{111\}< 112 >$ blocks are prone to microcracks nucleation due to their different deformation behavior (mismatch of Taylor factor) and higher local density of HABs resulting in a region susceptible to local strain-hardening and pill-ups of dislocations. Following the arrangement of the small grains, the microcracks can also nucleate lined up with each other as.

indicated in Fig. 12 **(b)**, **12 (f)**, and **14 (d)**. Moreover, the shear bands are regions containing mostly spheroidized cementite as presented in Fig. 10, which is supposed to have less resistance to the growth of microcracks. So, the microcracks may grow and connect themselves easily through the shear bands' path as pointed out in Fig. 12 **(f)**. Regarding the tensile gradient imposed by the bending state, the connection between two aligned microcracks likely happened through the growth of the more external microcrack (closer to the external surface of the specimen under tensile stress) in direction of the internal one (farther from the external surface of the specimen under tensile stress). However, the external microcrack growth can be hindered by fully lamellar pearlitic colonies orientated near the perpendicular direction of the crack propagation (see Fig. 12 **(f)** and **(g)**). In this case, the most internal defect can bend the pearlitic lamellae in the opposite direction of crack growth reaching the hindered microcrack. It may also occur due to the tensile gradient of the bending condition that facilitates the internal microcrack to overcome the lamellar obstacle.

4. Conclusions

Regarding the four lab-simulated process routes performed in this work which were based on the manufacture of pearlitic steel for tensile armor application, the present study evaluated the influence of key process parameters on the microstructure, microtexture, and crack susceptibility in pearlitic steel. In this context, the following conclusions can be drawn:

- The employment of patenting treatment in pearlitic steel tended to refine the pearlitic microstructure developing a weak ferritic Goss microtexture component, increasing the volume fraction of the ferritic grain boundary, and raising the microhardness.
- The refinement and homogenization efficiency of the pearlitic microstructure during the patenting treatment was mainly dependent on the arrangement of austenitization temperature and specimen thickness, regarding a constant austenitization holding time and bath salt temperature. Additionally, the adoption of cold deformation before the patenting treatment achieved the great refinement of pearlitic blocks.
- The patenting treatment affected the development of the $\{111\}< 112 >$ microtexture component during the cold-rolling process by controlling the initial pearlitic block size before the cold deformation.
- Stress relief treatment at 700 °C for 60 s applied in cold rolled pearlitic steel with the strongest $\{111\}< 112 >$ microtexture component resulted in small recrystallized grains nucleating in the shear bands of the $\{111\}< 112 >$ deformed pearlitic blocks and partial cementite spheroidization. Otherwise, no significant microstructural modifications were noticed when the stress relief was performed at 400 °C for 60 s
- Cracks and microcracks detected after the three-point bending experiment were found to nucleate between small recrystallized ferritic grains inside the $\{111\}< 112 >$ pearlitic blocks. Also, the microcracks seemed to be connected mainly via the shear bands' path. Finally, fully lamellar pearlite perpendicular orientated to the crack propagation was the only obstacle detected to hinder the microcrack growth.

Funding

This work was supported by the Coordenaç ão de Aperfeiçoamento de Pessoal de Nível Superior – Brasil (CAPES) [Finance Code 001].

CRediT authorship contribution statement

Pablo B. P. Leão: Conceptualization, Investigation, Visualization, Data curation, Writing – original draft, Writing – review & editing. **Shutong Zhang:** Software, Writing – review & editing. **J. R. Barros Neto:** Software, Formal analysis. **Suyanny A. Freire:** Validation, **Rodrigo de C. P. Loureiro:** Validation. **Antonio J. Ramirez:** Supervision, Funding acquisition. **H. F. G. de Abreu:** Supervision, Funding acquisition, Project administration.

Declaration of Competing Interest

The authors declare that they have no known competing financial interests or personal relationships that could have appeared to influence the work reported in this paper.

Data Availability

Data will be made available on request.

Acknowledgments

The authors acknowledge the support of the following facilities from the Universidade Federal do Ceará (UFC) and The Ohio State University (OSU): Laboratório de Caracterizaç ão de Materiais (LACAM), Central Analítica UFC/CT-INFRA FINEP/ProEquipamentos-CAPES/CNPq-SisNano-MCTI 2019 (Grant 442577/2019-2)-INCT-FUNCAP, the Manufacturing and Materials Joining Innovation Center (MA^2JIC), and the Center for Electron Microscopy and Analysis (CEMAS).

References

Aranda, M.M., Kim, B., Rementeria, R., Capdevila, C., García de Andrés, C., 2014. Effect of prior austenite grain size on pearlite transformation in a hypoeuctectoid Fe-C-Mn steel. Metall. Mater. Trans. A. 45, 1778–1786.
Arola, A.-M., Kaijalainen, A., Kesti, V., Troive, L., Larkiola, J., Porter, D., 2021. The effect of mechanical behavior on bendability of ultrahigh-strength steel. Mater. Today Commun. 26, 101943.
Bai, Y., Bai, Q. 2005. Subsea pipelines and risers, first ed. Elsevier, Oxford.
Barik, R.K., Ghosh, A., Sk, Md.B., Biswal, S., Dutta, A., Chakrabarti, D., 2021. Bridging microstructure and crystallography with the micromechanics of cleavage fracture in a lamellar pearlitic steel. Acta Mater. 214, 116988.
Behera, S., Barik, R.K., Sk, M.B., Mitra, R., Chakrabarti, D., 2019. Recipe for improving the impact toughness of high-strength pearlitic steel by controlling the cleavage cracking mechanisms. Mater. Sci. Eng. A. 764, 138256.

Bhole, S.D., Friedman, J.A., 2014. Steel wire patenting: thermal and metallurgical comparison between quenching in lead and quenching in a fluidised bed. IHTSE 4, 152–155.

Das, S., Ghosh, A., Chatterjee, S., Rao, P.R., 2003. The effect of cooling rate on structure and properties of a HSLA forging. Scr. Mater. 48, 51–57.

Dey, I., Chandra, S., Saha, R., Ghosh, S.K., 2018. Effect of Nb micro-alloying on microstructure and properties of thermomechanically processed high carbon pearlitic steel. Mater. Charact. 140, 45–54.

Durgaprasad, A., Giri, S., Lenka, S., Sarkar, S.K., Biswas, A., Kundun, S., Mishra, S., Chandra, S., Doherty, R.D., Samajdar, I., 2018. Delamination of pearlitic steel wires: the defining role of prior-drawing microstructure. Metall. Mater. Trans. A 49, 2037–2047.

EP 0 232 558 B1, 1990. Europe patent specification: Process for manufacturing pearlitic steel wire.

EP 0 478 771 B1, 1996. Fascicule de brevet europeen: Procede d'elaboration de fils d'acier destines a la fabrication de conduites flexibles, fils d'acier obtenus par ce procede et conduites flexibles renforcees par de tels fils.

Eshelby, J.D., Frank, F.C., Nabarro, F.R.N., 1951. XLI. The equilibrium of linear arrays of dislocations. Philos. Mag. 42, 351–364.

Fernando, U.S., Davidson, M., Yan, K., Roy, M.J., Pirling, T., Withers, P.J., Francis, J.A. 2017. Evolution of residual stress in tensile armour wires of flexible pipes during pipe manufacture. In: Proceeding of the ASME 2017 36th International Conference on Ocean, Offshore and Arctic Engineering, Trondheim, Norway.

Figueiredo, R.B., Langdon, T.G., 2022. Effect of grain size on strength and strain rate sensitivity in metals. J. Mater. Sci. 57, 5210–5229.

Furuhara, T., Mizoguchi, T., Maki, T., 2005. Ultra-fine $(\alpha+\theta)$ duplex structure formed by cold rolling and annealing of pearlite. ISIJ Int. 45, 392–398.

Ghosh, A., Mishra, B., Das, S., Chatterjee, S., 2005. Microstructure, properties, and age hardening behavior of a thermomechanically processed ultralow-carbon cu-bearing high-strength steel. Metall. Mater. Trans. A 36, 703–713.

Guo, N., Song, B., Luan, B., Chen, Z., Liu, Q., 2014. Deformation bands in fully pearlitic steel during wire drawing. Sci. China Technol. Sci. 57, 796–803.

Haessner, F. 1978. Recrystallization of Metallic Materials, second ed. Verlag GmbH, Stuttgart, pp. 159.

Hu, X.H., Jain, M., Wu, P.D., Wilkinson, D.S., Mishra, R.K., 2010. A macro-micro-multi-level modeling scheme to study the effect of particle distribution on wrap-bendability of AA5754 sheet alloys. J. Mater. Process. Technol. 210, 1232–1242.

Humphreys, J. Rohrer, S.G., Rollett, A. 2017. Recrystallization and related annealing phenomena recrystallization and related annealing phenomena, third ed. Elsevier, Amsterdam.

Javaheri, V., Sadeghpour, S., Kaijalainen, A., Kamali, M.R., Komi, J., 2021. Effect of post-rolling cooling on the hot-rolled microstructure and texture of a new medium-carbon steel. IOP Conf. Ser.: Mater. Sci. Eng.

Jazaeri, H., Humphreys, F.J., 2004. The effect of initial grain size on the microstructures developed during cold rolling of a single-phase aluminium alloy. MSF 467–470, 63–68.

Kanie, A., Tomota, Y., Torii, S., Kamiyama, T., 2004. Elastic strains of cementite in a pearlite, steel during tensile deformation measured by neutron diffraction. ISIJ Int. 44, 1952–1956.

Kapp, M.W., Renk, O., Eckert, J., Pippan, R., 2022. The importance of lamellar architecture to obtain ductility in heavily cold-worked pearlitic steels revealed by microbending experiments. Acta Mater. 232, 117935.

Kestens, L., Jacobs, S., 2008. Texture control during the manufacturing of nonoriented electrical steels. Texture Stress Microstruct., 173083

Kestens, L.A.I., Pirgazi, H., 2016. Texture formation in metal alloys with cubic crystal structures. Mater. Sci. Technol. 32, 1303–1315.

Leão, P.B.P., Medeiros, S.L.S., Saraiva, B.R.C., Barros Neto, J.R., Silva, C.C., Ramirez, A. J., de Abreu, H.F.G., 2022. Recrystallization kinetics and yield-strength adjustment after annealing of cold-rolled microalloyed steel. Mater. Sci. Technol. 38, 363–376.

Lewandowski, J.J., Thompson, A.W., 1986. Effects of the prior austenite grain size on the ductility of fully pearlitic eutectoid steel. Metall. Mater. Trans. A 17, 461–472.

Li, Y.J., Choi, P., Borchers, C., Westerkamp, S., Goto, S., Raabe, D., Kirchheim, R., 2011. Atomic-scale mechanisms of deformation-induced cementite decomposition in pearlite. Acta Mater. 59, 3965–3977.

Liu, M., Yang, C.D., Cao, G.H., Russell, Liu, A.M., Dong, X.M., Zhang, Z.H., 2016. Effect of microstructure and crystallography on sulfide stress cracking in API-5CT-C110 casing steel. Mater. Sci. Eng. A. 671, 244–253.

Lupton, D.F., Warrington, D.H., 1972. The influence of deformation on the spheroidization and coarsening of pearlite. Met. Sci. J. 6, 200–204.

Mandal, S., Tewary, N.K., Ghosh, S.K., Chakrabarti, D., Chatterjee, S., 2016. Thermo-mechanically controlled processed ultrahigh strength steel: microstructure, texture and mechanical properties. Mater. Sci. Eng. A 663, 126–140.

Miyamoto, G., Karube, Y., Furuhara, T., 2016. Formation of grain boundary ferrite in eutectoid and hypereutectoid pearlitic steels. Acta Mater. 103, 370–381.

Montana, Y., Idoyaga, Z., Gutiérrez, I., Iza-Mendia, A., 2022. Pearlite spheroidisation and microstructure refinement through heavy warm deformation of hot rolled 55VNb microalloyed steel. Metall. Mater. Trans. A. 53, 2586–2599.

Ohba, H., Tarui, T., Sugimoto, M., Hikita, N., Nishida, S., Yoshimura, K., Matsuoka, K. 2007. Nippon Steel Technical Report: High-performance Wire Rods Produced with DLP. 96.

Paris, H., 1996. Metallurgy, Processing and Applications of Metal Wires - A Review. TMS, Warrendale, pp. 3–15.

Porcaro, R.R., Faria, G.L., Godefroid, L.B., Apolonio, G.R., Cândido, L.C., Pinto, E.S., 2019. Microstructure and mechanical Properties of a flash butt welded pearlitic rail. J. Mater. Process. Technol. 270, 20–27.

Saastamoinen, A., Kaijalainen, A., Porter, D., Suikkanen, P., 2017. The effect of thermomechanical treatment and tempering on the subsurface microstructure and bendability of direct-quenched low-carbon strip steel. Mater. Charact. 134, 172–181.

Saito, R., Nakada, N., Yabu, S., Hayashi, K., 2018. Effects of initial structure and reversion temperature on austenite nucleation site in pearlite and ferrite-pearlite. Metall. Mater. Trans. A. 49, 6001–6009.

Sun, J.-J., Lian, F.-L., Liu, H.-J., Jiang, T., Guo, S.-W., Du, L.-X., Liu, Y.-N., 2014. Microstructure of warm rolling and pearlitic transformation of ultrafine-grained GCr15 steel. Mater. Charact. 95, 291–298.

Szpunar, J.A., Basu, R., Eskandari, M., 2015. The mechanism of failure by hydrogen induced cracking in an acidic environment for API, 5L X70 pipeline steel. Hydrog. Energy 40, 1096–1107.

Tagashira, S., Sakai, K., Furuhara, T., Maki, T., 2000. Deformation microstructure and tensile strength of cold rolled pearlitic steel sheets. ISIJ Int. 40, 1149–1155.

Tagliari, M.R., Antunes, M.R., dos Santos, J.G.N., dos Santos, F.P., dos Santos, J.M.C., Falcade, T., Reguly, A., 2019. Tensile armor wires submitted to slow strain rate tests in a corrosive environment and cathodic protection: a comparison between two different microstructures. Mater. Res. 22.

Takahashi, T., Nagumo, M., Asano, Y., 1978a. Crystallographic features and formation processes of pearlite block. J. Jpn. Inst. Met. 42, 716–723.

Takahashi, T., Nagumo, M., Asano, Y., 1978b. Crystallographic features and formation processes of pearlite block. J. Jpn. Inst. 42, 716–723.

Taleff, E.M., Lewandowski, J.J., Pourladian, B., 2002. Microstructure-property relationships in pearlitic eutectoid and hypereutectoid carbon steels. JOM 54, 25–30.

Teshima, T., Kosaka, M., Ushioda, K., Koga, N., Nokada, N., 2017. Local cementite cracking induced by heterogeneous plastic deformation in lamellar pearlite. Mater. Sci. Eng. A 679, 223–229.

Tomota, Y., Watanabe, O., Kanie, A., Moriai, A., Minakawa, N., Moriai, Y., 2003. Effect of carbon concentration on tensile behavior of pearlitic steels. Mater. Sci. Technol. 19, 1715–1720.

Tóth, L.S., Jonas, J.J., Daniel, D., Ray, R.K., 1990. Development of ferrite rolling textures in low- and extra low-carbon steels. Metall. Trans. 21, 2985–3000.

Umar, M., Qayyum, F., Farooq, M.U., Khan, L.A., Guk, S., Prahl, U., 2021. Investigating the effect of cementite particles size and distribution on local stress and strain evolution in spheroidized medium carbon steel using crystal plasticity-based numerical simulations. Steel Res. Int. 92, 2000407.

US 9.249.486 B2, 2016. United States Patent: Profiled steel wire with high mechanical characteristics resistant to hydrogen embrittlement.

Valiente, A., Ruiz, J., Elices, M., 2005. A probabilistic model for the pearlite-induced cleavage of a plain carbon structural steel. Eng. Fract. Mech. 72, 709–728.

Waterschoot, T., Kestens, L., De Cooman, B.C., 2002. Hot rolling texture development in CMnCrSi dual-phase steels. Metall. Mater. Trans. A 33, 1091–1102.

Wright, S., Nowell, M., Field, D., 2011. A review of strain analysis using electron backscatter diffraction. Microsc. Microanal. 17, 316–329.

Yajima, Y., Koga, N., Watanabe, C., 2021. Influential factors on the deformability of colonies in pearlitic steel. Mater. Charact. 177, 111197.

Yan, N., Li, Z., Xu, Y., Meyers, M.A., 2021. Shear localization in metallic materials at high strain rates. Prog. Mater. Sci. 119, 100755.

Zhang, X., Wang, C.X., Liu, X.M., Shi, Q.N., 2007. Microstructure evolution and mechanical hardening of hypereutectoid pearlitic steel during cold rolling. Acta Metall. Sin. -Engl. 20, 287–292.

Zhao, X.-Y., Zhao, X.-M., Dong, C.-Y., Yang, Y., Han, H.-B., 2022. Effect of prior microstructures on cementite dissolution behavior during subcritical annealing of high carbon steels. Met. Mater. Int. 28, 1315–1327.

Zhou, S., Zuo, Y., Li, Z., Wang, Z., Yong, Q., 2016. Microstructural analysis on cleavage fracture in pearlitic steels. Mater. Charact. 119, 110–113.